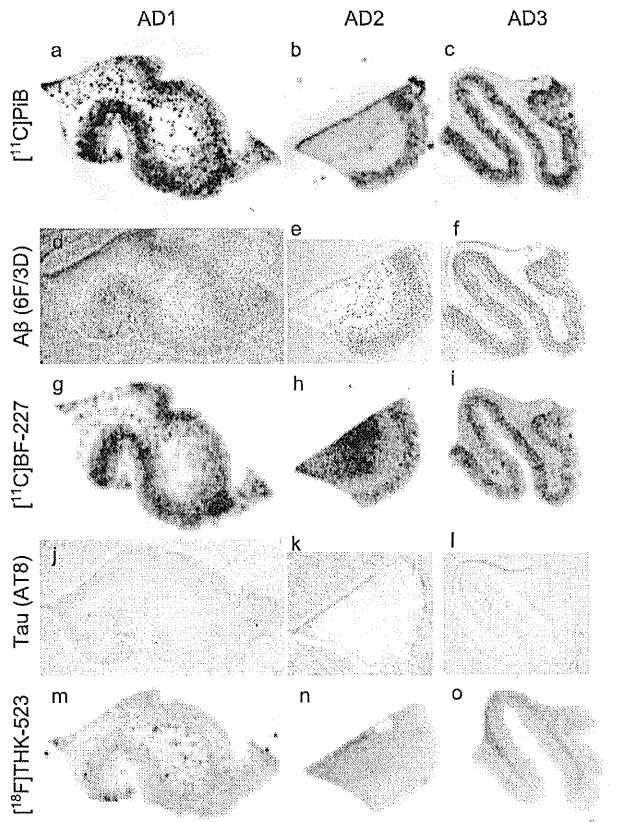

Fig. 2 Comparison of [^{11}C]PiB, [^{11}C]BF-227 and [^{18}F]THK-523 autoradiography with the Aβ and tau immunostaining in sections of the frontal brain from three patients with AD (*AD1*, *AD2*, *AD3*). Both [^{11}C]PiB (**a–c**) and [^{11}C]BF-227 (**g–i**) showed dense accumulation in the grey matter, closely resembling the pattern of Aβ immunohistochemistry using the 6F/3D antibody (**d–f**). [^{18}F]THK-523 (**m–o**) did not accumulate in the grey matter, which was correlated with no marked staining with anti-tau antibody AT8 (**j–l**)

candidate as a tau imaging tracer, and could also be a lead compound for future development of tau-selective radiotracers. We speculate that [^{18}F]THK-523 would show retention in tau-rich brain regions if administered to AD patients. However, the specific signal of [^{18}F]THK-523 might be lower than those of PiB and BF-227 owing to the lower amount of tau deposits in the neocortex of AD patients [27]. Further compound optimization may be required to achieve higher contrast imaging of PHF-tau deposits.

In in vitro saturation binding studies [^{18}F]THK-523 bound with higher affinity to tau fibrils (K_{D1} 1.99 nM) than to $A\beta_{42}$ fibrils (K_{D1} 30.3 nM), whereas PiB and BF-227 showed the opposite binding characteristics. [^{3}H]PiB bound with higher affinity to $A\beta_{42}$ fibrils (K_{D1} 0.84 nM) than to tau fibrils (K_{D1} 6.39 nM), similar to previous reports [7, 28, 29], and [^{18}F]BF-227 had more than a tenfold higher affinity for $A\beta_{42}$ fibrils (K_{D1} 1.72 nM) than for tau fibrils (K18ΔK280; K_{D1} 30.2 nM). Autoradiographic images of sections of AD brain revealed that [^{11}C]PiB and [^{11}C]BF-227 accumulated in the grey matter of the neocortex, which closely resembled the staining pattern of Aβ immunohistochemistry. A previous study suggested that [^{3}H]PiB labelled NFTs at tracer concentrations usually achieved during a PET scan [13]. However, another study showed no binding of the PiB derivative [^{3}H]BTA-1 to

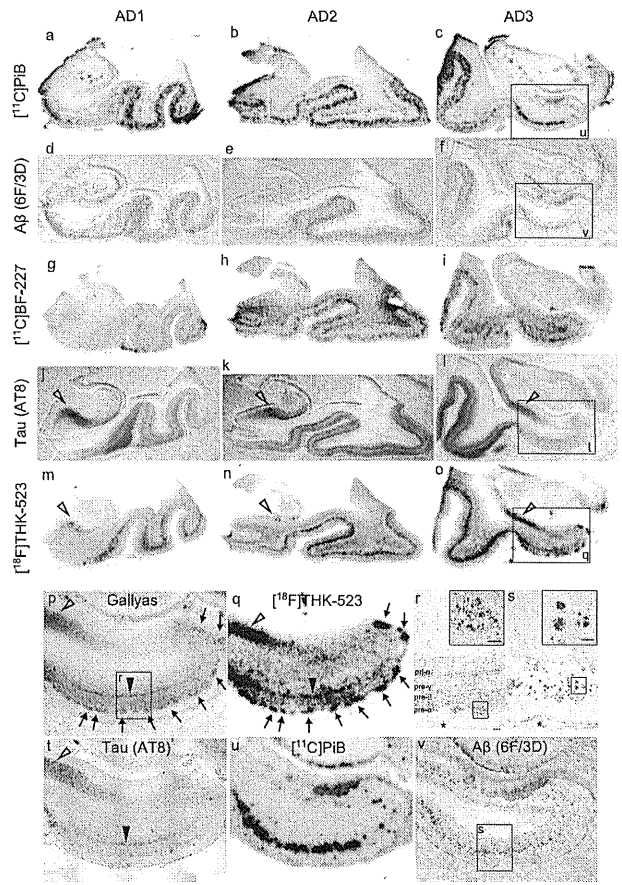

Fig. 3 Comparison of [^{11}C]PiB, [^{11}C]BF-227 and [^{18}F]THK-523 autoradiography with Aβ and tau immunostaining images in sections of the medial temporal brain from three patients with AD (*AD1*, *AD2*, *AD3*). [^{11}C]PiB (**a–c**) and [^{11}C]BF-227 (**g–i**) do not accumulate in the hippocampal CA1 area which contains a low density of Aβ (**d–f**). In contrast, accumulation of [^{18}F]THK-523 is observed in the hippocampal CA1 area (**m–o**, *arrowheads*), which closely resembles AT8 immunoreactivity (**j–l**, *arrowheads*). In addition, the band-like labelling pattern of [^{18}F]THK-523 in the inner layer of temporal cortex (**m–o**) is closely similar to that of AT8 immunostaining (**j–l**). **p–v** High magnification images of the medial temporal sections from patient AD3. Many clusters of [^{18}F]THK-523 binding in the ERC are consistent with Gallyas silver staining (**p**, **q**, *arrows*). **r** Close-up image from **p**. Numerous NFTs are located in the layer pre-α of the ERC (**r** *inset*). The band-like distribution of [^{18}F]THK-523 in the layer pri-α of the ERC also resembles the labelling pattern of Gallyas silver staining (**p**, *filled arrowhead*) as well as AT8 immunoreactivity (**t**, *filled arrowhead*). [^{11}C]PiB binding (**u**) is also present in the ERC, but obviously different from [^{18}F]THK-523 binding (**q**) and similar to the 6F/3D immunostaining pattern (**v**). Lake-like amyloid in the presubicular region (**v**) is labelled with [^{11}C]PiB, but not with [^{18}F]THK-523. **s** Close-up image from **v**. Aβ plaques (**s** *inset*) located in the layer pre-β and pre-γ are intensely labelled with [^{11}C]PiB (**u**). *Asterisks* in **r** and **s** denote the same large blood vessel. *Scale bar* 100 μm

plaque-free and NFT-rich ERC homogenates, despite the high amount of [^{3}H]BTA-1 binding to frontal cortex homogenates containing high levels of neuritic plaques [30]. Autoradiographic and immunohistochemical analyses indicated that PiB predominantly binds to senile plaques but not to NFTs. These findings are consistent with the findings from clinical PiB-PET studies showing no remarkable PiB retention in the medial temporal cortex of AD patients [7].

Another radiotracer, [^{18}F]FDDNP, has been reported to detect Aβ and tau pathological lesions in AD patients [3]. Previous clinical PET studies have shown higher cortical uptake of [^{18}F]FDDNP in the lateral and medial temporal lobes of AD subjects [3, 5]. Furthermore, a multitracer PET study of [^{11}C]PiB and [^{18}F]FDDNP has shown significant retention of FDDNP in the medial temporal cortex, albeit no remarkable retention of PiB in the same region [31]. However, in vitro binding studies have shown the limited binding affinity of [^{3}H]FDDNP to AD pathological lesions [24], and a previous autoradiographic analysis has suggested that [^{3}H]FDDNP does not significantly label any region in AD brain [24]. Previous in vitro binding studies additionally showed the binding affinity of FDDNP for $A\beta_{40}$ fibrils (K_D 0.12, 85 nM) [19, 24], but the binding affinity for tau fibrils was not reported. Here, we showed that the binding affinity of [^{18}F]FDDNP for tau fibrils (K_{D1} 36.7 nM) was similar to that of [^{18}F]BF-227 (K_{D1} 30.2 nM), but much higher than that of [^{18}F]THK-523 (K_{D1} 1.99 nM).

In conclusion, the binding profiles of [^{18}F]THK-523, [^{11}C]PiB, [^{18}F]BF-227, and [^{18}F]FDDNP were compared using in vitro saturation binding assays and autoradiography of sections of AD brain. These data suggest that [^{18}F]THK-523 shows a binding preference for tau protein fibrils. Therefore, [^{18}F]THK-523 is a candidate as a radiotracer to identify tau protein deposits and a lead compound for future tracer development. Ongoing clinical trials will clarify the clinical utility of this tracer and its derivatives for tau imaging in vivo.

Acknowledgments This study was supported by the Industrial Technology Research Grant Program of the NEDO in Japan, Health and Labor Sciences Research Grants from the Ministry of Health, Labor, and Welfare of Japan, and Grant-in-Aid for Scientific Research (B) (23390297).

References

1. Nordberg A, Rinne JO, Kadir A, Langstrom B. The use of PET in Alzheimer disease. Nat Rev Neurol. 2010;6:78–87. doi:10.1038/nrneurol.2009.217.
2. Furumoto S, Okamura N, Iwata R, Yanai K, Arai H, Kudo Y. Recent advances in the development of amyloid imaging agents. Curr Top Med Chem. 2007;7:1773–89.
3. Shoghi-Jadid K, Small GW, Agdeppa ED, Kepe V, Ercoli LM, Siddarth P, et al. Localization of neurofibrillary tangles and beta-amyloid plaques in the brains of living patients with Alzheimer disease. Am J Geriatr Psychiatry. 2002;10:24–35.
4. Mathis CA, Wang Y, Holt DP, Huang GF, Debnath ML, Klunk WE. Synthesis and evaluation of 11C-labeled 6-substituted 2-arylbenzothiazoles as amyloid imaging agents. J Med Chem. 2003;46:2740–54. doi:10.1021/jm030026b.
5. Klunk WE, Engler H, Nordberg A, Wang Y, Blomqvist G, Holt DP, et al. Imaging brain amyloid in Alzheimer's disease with Pittsburgh Compound-B. Ann Neurol. 2004;55:306–19. doi:10.1002/ana.20009.
6. Kudo Y, Okamura N, Furumoto S, Tashiro M, Furukawa K, Maruyama M, et al. 2-(2-[2-Dimethylaminothiazol-5-yl]ethenyl)-6- (2-[fluoro]ethoxy)benzoxazole: a novel PET agent for in vivo detection of dense amyloid plaques in Alzheimer's disease patients. J Nucl Med. 2007;48:553–61.
7. Ikonomovic MD, Klunk WE, Abrahamson EE, Mathis CA, Price JC, Tsopelas ND, et al. Post-mortem correlates of in vivo PiB-PET amyloid imaging in a typical case of Alzheimer's disease. Brain. 2008;131:1630–45. doi:10.1093/brain/awn016.
8. Sperling RA, Aisen PS, Beckett LA, Bennett DA, Craft S, Fagan AM, et al. Toward defining the preclinical stages of Alzheimer's disease: recommendations from the National Institute on Aging-Alzheimer's Association workgroups on diagnostic guidelines for Alzheimer's disease. Alzheimers Dement. 2011;7:280–92. doi:10.1016/j.jalz.2011.03.003.
9. Jack Jr CR, Knopman DS, Jagust WJ, Shaw LM, Aisen PS, Weiner MW, et al. Hypothetical model of dynamic biomarkers of the Alzheimer's pathological cascade. Lancet Neurol. 2010;9:119–28. doi:10.1016/S1474-4422(09)70299-6.
10. Pike KE, Savage G, Villemagne VL, Ng S, Moss SA, Maruff P, et al. Beta-amyloid imaging and memory in non-demented individuals: evidence for preclinical Alzheimer's disease. Brain. 2007;130:2837–44. doi:10.1093/brain/awm238.
11. Okamura N, Suemoto T, Furumoto S, Suzuki M, Shimadzu H, Akatsu H, et al. Quinoline and benzimidazole derivatives: candidate probes for in vivo imaging of tau pathology in Alzheimer's disease. J Neurosci. 2005;25:10857–62. doi:10.1523/JNEUROSCI.1738-05.2005.
12. Fodero-Tavoletti MT, Okamura N, Furumoto S, Mulligan RS, Connor AR, McLean CA, et al. 18F-THK523: a novel in vivo tau imaging ligand for Alzheimer's disease. Brain. 2011;134:1089–100. doi:10.1093/Brain/Awr038.
13. Lockhart A, Lamb JR, Osredkar T, Sue LI, Joyce JN, Ye L, et al. PIB is a non-specific imaging marker of amyloid-beta (Abeta) peptide-related cerebral amyloidosis. Brain. 2007;130:2607–15. doi:10.1093/brain/awm191.
14. Buraek MA, Hartlein J, Flores HP, Taylor-Reinwald L, Perlmutter JS, Cairns NJ. In vivo amyloid imaging in autopsy-confirmed Parkinson disease with dementia. Neurology. 2010;74:77–84. doi:10.1212/WNL.0b013e3181c7da8e.
15. Clark CM, Schneider JA, Bedell BJ, Beach TG, Bilker WB, Mintun MA, et al. Use of florbetapir-PET for imaging beta-amyloid pathology. JAMA. 2011;305:275–83. doi:10.1001/jama.2010.2008.
16. Wong DF, Moghekar AR, Rigamonti D, Brasic JR, Rousset O, Willis W, et al. An in vivo evaluation of cerebral cortical amyloid with [(18)F]Flutemetamol using positron emission tomography compared with parietal biopsy samples in living normal pressure hydrocephalus patients. Mol Imaging Biol. 2012. doi:10.1007/s11307-012-0583-x.
17. Maeda J, Ji B, Irie T, Tomiyama T, Maruyama M, Okauchi T, et al. Longitudinal, quantitative assessment of amyloid, neuroinflammation, and anti-amyloid treatment in a living mouse model of Alzheimer's disease enabled by positron emission tomography. J Neurosci. 2007;27:10957–68. doi:10.1523/JNEUROSCI.0673-07.2007.

18. Manook A, Yousefi BH, Willuweit A, Platzer S, Reder S, Voss A, et al. Small-animal PET imaging of amyloid-beta plaques with [11C]PiB and its multi-modal validation in an APP/PS1 mouse model of Alzheimer's disease. PLoS One. 2012;7:e31310. doi:10.1371/journal.pone.0031310.
19. Agdeppa ED, Kepe V, Liu J, Flores-Torres S, Satyamurthy N, Petric A, et al. Binding characteristics of radiofluorinated 6-dialkylamino-2-naphthylethylidene derivatives as positron emission tomography imaging probes for beta-amyloid plaques in Alzheimer's disease. J Neurosci. 2001;21:RC189.
20. Gallyas F. Silver staining of Alzheimer's neurofibrillary changes by means of physical development. Acta Morphol Acad Sci Hung. 1971;19:1–8.
21. Barghorn S, Davies P, Mandelkow E. Tau paired helical filaments from Alzheimer's disease brain and assembled in vitro are based on beta-structure in the core domain. Biochemistry. 2004;43:1694–703. doi:10.1021/bi0357006.
22. von Bergen M, Barghorn S, Muller SA, Pickhardt M, Biernat J, Mandelkow EM, et al. The core of tau-paired helical filaments studied by scanning transmission electron microscopy and limited proteolysis. Biochemistry. 2006;45:6446–57. doi:10.1021/bi052530j.
23. Fodero-Tavoletti MT, Mulligan RS, Okamura N, Furumoto S, Rowe CC, Kudo Y, et al. In vitro characterisation of BF227 binding to alpha-synuclein/Lewy bodies. Eur J Pharmacol. 2009;617:54–8. doi:10.1016/j.ejphar.2009.06.042.
24. Thompson PW, Ye L, Morgenstern JL, Sue L, Beach TG, Judd DJ, et al. Interaction of the amyloid imaging tracer FDDNP with hallmark Alzheimer's disease pathologies. J Neurochem. 2009;109:623–30. doi:10.1111/j.1471-4159.2009.05996.x.
25. Braak E, Braak H, Mandelkow EM. A sequence of cytoskeleton changes related to the formation of neurofibrillary tangles and neuropil threads. Acta Neuropathol. 1994;87:554–67.
26. Thal DR, Rub U, Schultz C, Sassin I, Ghebremedhin E, Del Tredici K, et al. Sequence of Abeta-protein deposition in the human medial temporal lobe. J Neuropathol Exp Neurol. 2000;59:733–48.
27. Villemagne VL, Furumoto S, Fodero-Tavoletti M, Harada R, Mulligan RS, Kudo Y, et al. The challenges of tau imaging. Future Neurol. 2012;7:409–21. doi:10.2217/fnl.12.34.
28. Fodero-Tavoletti MT, Smith DP, McLean CA, Adlard PA, Barnham KJ, Foster LE, et al. In vitro characterization of Pittsburgh compound-B binding to Lewy bodies. J Neurosci. 2007;27:10365–71. doi:10.1523/JNEUROSCI.0630-07.2007.
29. Klunk WE, Lopresti BJ, Ikonomovic MD, Lefterov IM, Koldamova RP, Abrahamson EE, et al. Binding of the positron emission tomography tracer Pittsburgh compound-B reflects the amount of amyloid-beta in Alzheimer's disease brain but not in transgenic mouse brain. J Neurosci. 2005;25:10598–606. doi:10.1523/JNEUROSCI.2990-05.2005.
30. Klunk WE, Wang Y, Huang GF, Debnath ML, Holt DP, Shao L, et al. The binding of 2-(4'-methylaminophenyl)benzothiazole to post-mortem brain homogenates is dominated by the amyloid component. J Neurosci. 2003;23:2086–92.
31. Shin J, Lee SY, Kim SH, Kim YB, Cho SJ. Multitracer PET imaging of amyloid plaques and neurofibrillary tangles in Alzheimer's disease. Neuroimage. 2008;43:236–44. doi:10.1016/j.neuroimage.2008.07.022.

Dig Dis Sci (2012) 57:2965–2974
DOI 10.1007/s10620-012-2165-9

ORIGINAL ARTICLE

A Shift from Colon- to Ileum-Predominant Bacteria in Ileal-Pouch Feces Following Total Proctocolectomy

Manami Hinata · Atsushi Kohyama · Hitoshi Ogawa · Sho Haneda · Kazuhiro Watanabe · Hideyuki Suzuki · Chikashi Shibata · Yuji Funayama · Ken-ichi Takahashi · Iwao Sasaki · Kouhei Fukushima

Received: 16 October 2011 / Accepted: 3 April 2012 / Published online: 27 April 2012

Abstract
Background We previously investigated fecal flora of the pouch after total proctocolectomy using terminal restriction fragment polymorphism analysis. Although the results of the cluster analysis demonstrated clearly that bacterial populations, including an unidentified bacteria generating a 213-bp PCR fragment, moved toward a colon-like community in the pouch, it did not track changes in the individual species of fecal bacteria.
Aims The aim of the present study was to estimate genome copy number of ten bacterial species, clusters, groups, or subgroups (including the bacteria generating 213-bp fragment in the previous study) in feces samples from pouches at various times following ileostomy closure.
Methods A total of 117 stool samples were collected from patients with ulcerative colitis after surgery as well as healthy volunteers. We used real-time polymerase chain reaction of the 16S rRNA gene to estimate genome copy numbers for the nine bacterial populations and the bacteria generating 213-bp fragment after identification by DNA sequencing.
Results We demonstrated a time-dependent increase in the number of anaerobic and colon-predominant bacteria (such as *Clostridium coccoides*, *C. leptum*, *Bacteroides fragilis* and *Atopobium*) present in proctocolectomy patients after stoma closure. In contrast, numbers of ileum-predominant bacterial species (such as *Lactobacillus* and *Enterococcus faecalis*) declined.
Conclusions Our data confirm previous findings that fecal flora in the pouch after total proctocolectomy changes significantly, and further demonstrate that the number and diversity of ileal bacteria decreases while a more colon-like community develops. The present data are essential for the future analysis of pathological conditions in the ileal pouch.

Keywords Ulcerative colitis · Restorative proctocolectomy · Pouchitis · Microbiota · Intestines

M. Hinata · K. Fukushima (✉)
Division of Molecular and Surgical Pathophysiology, Graduate School of Medicine, Tohoku University, 2-1 Seiryo-machi, Aoba-ku, Sendai 980-8575, Japan
e-mail: kouhei@surg1.med.tohoku.ac.jp

A. Kohyama · H. Ogawa · S. Haneda · K. Watanabe · H. Suzuki · C. Shibata · I. Sasaki
Division of Biological Regulation and Oncology, Department of Surgery, Graduate School of Medicine, Tohoku University, 1-1 Seiryo-machi, Aoba-ku, Sendai 980-8574, Japan
e-mail: akoyama@east.ncc.go.jp

H. Ogawa
e-mail: hogawa@surg1.med.tohoku.ac.jp

S. Haneda
e-mail: sho@surg1.med.tohoku.ac.jp

K. Watanabe
e-mail: k-wata@surg1.med.tohoku.ac.jp

H. Suzuki
e-mail: hideji@surg1.med.tohoku.ac.jp

C. Shibata
e-mail: cshibata@surg1.med.tohoku.ac.jp

I. Sasaki
e-mail: isasaki@surg1.med.tohoku.ac.jp

Y. Funayama · K. Takahashi
Division of Colorectal and Anal Diseases, Tohoku Rosai Hospital, 4-3-21, Dainohara, Aoba-ku, Sendai 981-8563, Japan
e-mail: yfunayama@tohokuh.rofuku.go.jp

K. Takahashi
e-mail: kentaka@tohokuh.rofuku.go.jp

K. Fukushima
Laboratory of Gastrointestinal Tract, Department of Regenerative Medicine, Graduate School of Biomedical Engineering, Tohoku University, Sendai, Japan

Introduction

Total proctocolectomy (TPC) followed by ileal pouch-anal anastomosis (IPAA) is an established surgical treatment for ulcerative colitis (UC) and familial adenomatous polyposis (FAP). Removal of the entire colon enables patients to be cured of disease without construction of a permanent ileostomy. Postoperative adaptive change in the intestine, termed "intestinal adaptation," is thought to be advantageous for maintaining homeostasis. A previous report involving microarray data derived from isolated epithelial cells described intestinal adaptation as a colon-like transformation of ileal epithelia (i.e. ileal epithelial cells assume a partial colonic phenotype and lose characteristics of the ileal phenotype) [1]. One functional result of adaptation is enhanced water and electrolyte absorption in the remnant small intestine over time, changing stool consistency from watery diarrhea to paste stool.

Beside changes in the water content of stool, intestinal adaptation also involves changes in the composition of fecal microbiota. In a previous study, we used terminal restriction fragment length polymorphism (T-RFLP) analysis to investigate changes in fecal flora at various times after total proctocolectomy, sampling both culturable and nonculturable fecal bacteria [2]. These T-RFLP data led us to define "ileal" DNA fragments as those that were both (a) detected in more than 70 % of ileostomy fecal samples and (b) present at a significantly greater frequency ($p < 0.05$) in ileostomy samples relative to control feces. In contrast, we defined signature "colonic" DNA fragments as those (a) identified in more than 70 % of control samples and (b) present at a significantly greater concentration ($p < 0.05$) in control feces relative to ileostomy samples [2]. T-RFLP patterns derived from ileal-pouch fecal DNA samples showed both a time-dependent decrease in the relative abundance of "ileal" fragments and a time-dependent increase in "colonic" DNA fragments (derived mainly from nonculturable bacteria). One specific 213-bp fragment that decreased in abundance after TPC/IPAA (an "ileal" signature) was sequenced and showed no matches within current sequence databases, suggesting identification of a novel bacterium that may contribute to adaptation [2].

Traditional methods for determining the composition of intestinal microbiota require time-consuming and laborious culture techniques. While T-RFLP allows a more rapid and complete assessment of bacterial community diversity, this molecular approach does not accurately measure quantities of individual bacteria, and also can "miss" detecting DNAs from very small numbers of target bacteria. For these reasons, additional methods beyond T-RFLP are necessary to accurately detect and quantify populations of major and minor bacteria. While detection of specific-size molecular fragments provides clues to the presence of a bacterial species, procedures are required to compare and confirm the sequence of the fragment relative to the putative origin species. Alternative methods are also required for further analysis of any restriction fragment without a database match.

Real-time polymerase chain reaction (real-time PCR) has been used successfully to quantify small amounts of bacterial DNA from various samples, including feces [3, 4]. In this study, we estimated population sizes of fecal bacteria in UC patients after IPAA using real-time PCR analysis. We applied an extensive set of ten primer pairs designed to target 16S rRNA genes from species, genera, groups, and subgroups that are either (a) common in fecal flora, (b) predominant in the colon, (c) specific to "ileal" bacteria originating in the 213-bp "ileal" fragment after identification, or (d) found in conjunction with pouchitis (mucosal inflammation that develops in UC patients after IPAA).

In each case, detection of the genus *Desulfovibrios* served as a marker for pouchitis-associated flora. In a previous report, Ohge et al. found that release of hydrogen sulphide from feces increased and was significantly higher in patients with active pouchitis within the past year relative to patients in whom pouchitis never occurred or was inactive in the past year [5]. This is thought to be due to bacteria of the genus *Desulfovibrio* that reduce sulphate to sulphide, which is known to be toxic to colonic epithelial cells [6].

Materials and Methods

Samples

We obtained 117 stool samples from 69 patients and 20 healthy volunteers (Table 1). Diagnosis of UC was based on a combination of clinical symptoms, endoscopic findings and histological examination. All 69 UC patients underwent TPC followed by IPAA at Tohoku University Hospital, where two- or three-step surgeries were routine.

Table 1 Summary of samples

Time since ileostomy	No. of samples	No. of patients (male:female)	Mean age (range)
Ileostomy	16	16 (9:7)	38.6 (21–70)
<50 days	12	9 (8:1)	33.1 (23–55)
51–100 days	11	9 (6:3)	39.5 (23–55)
101 days–1 year	14	8 (6:2)	33.6 (17–50)
>1 year	44	27 (15:12)	40.7 (24–62)
Healthy volunteer	20	20 (8:12)	32.8 (18–55)
Total	117	89 (52:37)	37.0 (17–70)

Upon complete closure of the covering loop-ileostomy, the ileal pouch generally becomes functional and stool can be excreted from the patient's anus. Of the 20 healthy volunteers, 19 were not treated with any medications and one took anti-hypertension drugs daily. As depicted in Table 1, we categorized stool samples into one of six groups based on their site and time of origin: Samples were either (1) from end- or loop-ileostomy (16 samples) at 14 or 15 days after the initial surgery, (2) from an ileal pouch within 50 days after stoma closure (12 samples), (3) from an ileal pouch more than 51 days and within 100 days after stoma closure (11 samples), (4) from an ileal pouch more than 101 days and within 1 year after stoma closure (14 samples), (5) from an ileal pouch over 1 year after stoma closure (44 samples), or (6) from healthy volunteer controls (20 samples).

Fourteen of 16 ileostomy samples were obtained from patients who were treated with predonisolone (10–30 mg/day) and antibiotics (cefotiam hydrochloride, 2 g/day) until the fourth post-operative day. All samples in this study originated from patients with an ileal pouch, but who also were free from surgical complications and any clinical symptoms that might indicate pouchitis. In an additional analysis, we compared stool samples taken from each of seven patients at two different times: the first sampling one or more years after ileostomy closure, and the second sampling 1 year later.

Fecal samples from hospital outpatients were collected at each visit following excretion into toilets designed for sample collection. The samples were frozen immediately and then stored at −80 °C until the time of DNA extraction. Fecal samples were obtained under informed consent, and the study was approved by the Ethics Committee of Tohoku University, Graduate School of Medicine.

DNA Extraction from Fecal Samples

Stool DNA was extracted using QIAamp DNA Stool Mini Kit (QIAGEN Co., Tokyo, Japan) according to the manufacturer's protocol. The DNA concentration of each sample was estimated from its spectrophotometric absorbance of 260-nm wavelength light.

Preliminary PCR Amplification and Cloning of Control Plasmids for Real-Time PCR

PCR with bacteria-specific primer pairs (Table 2) was used to amplify 16S rRNA fragments from target bacteria and control plasmid standards for real-time PCR. Each reaction mixture (12.5 μl) included 10 ng DNA, 1× buffer supplied by the manufacturer, 0.2 mM NTP, 0.6 μM up- and downstream primers, and 0.3 unit TaKaRa Ex Taq (Takara Shuzo Co., Ltd., Otsu, Japan). DNA was initially denatured at 94 °C for 2 min, and then proceeded through 35 thermocycles of 94 °C for 30 s, 50 or 55 °C for 30 s, and 72 °C for 30 s, with a final extension period at 72 °C for 5 min. Resulting amplified products were resolved using gel electrophoresis and stained with ethidium bromide. Target DNAs of the expected size were cloned into pCR 2.1-TOPO (TOPO TA Cloning Kit, Invitrogen Co., Tokyo, Japan) according to the manufacturer's protocol. Plasmids from bacterial clones containing target DNA were purified using miniprep DNA Purification Kit (Takara Shuzo Co., Ltd.) and sequenced using BigDye Terminator v3.1 Cycle Sequence Kit (Applied Biosystems) during 25 thermocycles at 96 °C for 10 s, 50 °C for 5 s, and 60 °C for 4 min. The resulting products were purified using BigDye XTerminator and analyzed using an ABI310 sequencer (Applied Biosystems Japan, Tokyo, Japan).

Quantification of Bacterial DNAs Using Real-Time PCR

Duplicate samples of 10-ng bacterial DNA were used for 16S rRNA gene quantification with QuantiTect SYBR Green PCR Kit (Qiagen K. K.,Tokyo, Japan) (except for *Lactobacillus* species) and ABI 7500 Real-time PCR system (Applied Biosystems, Japan) according to the manufacturer's protocol. The amplification program consisted of one cycle of 50 °C for 2 min, one cycle of 95 °C for 10 min, 45 cycles of 94 °C for 15 s, 55 °C for 30 s, and 72 °C for 1 min. When *Enterococcus* species or *Enterococcus faecalis* was measured, the annealing temperature was 61 or 57 °C, respectively. Quantification in duplicate of *Lactobacillus* species was performed using EagleTaq

Table 2 Primer and probe sets used in this study

Target bacterial group	Primer sequence	Amplicon size (bp)	Reference
All eubacteria	TCCTACGGGAGGCAGCAGT	466	[7]
	GGACTACCAGGGTATCTATCCTGTT		
Clostridium coccoides group	AAATGACGGTACCTGACTAA	440	[3]
	CTTTGAGTTTCATTCTTGCGAA		
Clostridium leptum subgroup	GCACAAGCAGTGGAGT	239	[3]
	CTTCCTCCGTTTTGTCAA		
Bacteroides fragilis group	ATAGCCTTTCGAAAGRAAGAT	495	[3]
	CCAGTATCAACTGCAATTTTA		
Bifidobacterium	CTCCTGGAAACGGGTGG	550	[3]
	GGTGTTCTTCCCGATATCTACA		
Atopobium cluster	GGGTTGAGAGACCGACC	190	[3]
	CGGRGCTTCTTCTGCAGG		
Prevotella	CACRGTAAACGATGGATGCC	513	[3]
	GGTCGGGTTGCAGACC		
Desulfovibrios	CCGTAGATATCTGGAGGAACATCA	135	[8]
	ACATCTAGCATCCATCGTTTACAGC		
Lactobacillus species	TACATYCCAACHCCAGAACG	71	[9]
	AAGCAACAGTACCACGACCA		
	Probe: FAM- AAGCAACAGTACCACGACCA-TAMRA		
Enterococcus species	CCCTTATTGTTAGTTGCCATCATT	144	[4]
	ACTCGTTGTACTTCCCATTGT		
Enterococcus faecalis	AACCTACCCATCAGAGGG	358	[10]
	GACGTTCAGTTACTAACG		

Master Mix with ROX (Roche Diagnostics Co., Tokyo, Japan). The amplification program consisted of one cycle of 50 °C for 2 min, one cycle of 95 °C for 10 min, 45 cycles of 95 °C for 15 s, 60 °C for 1 min, and 72 °C for 1 min. Copy number per microgram stool DNA was calculated relative to plasmid DNA controls, and median and percentile values in each group were evaluated.

Isolation and Identification of the 213-bp Fragment

We used the AccuPrime Taq DNA polymerase system (Invitrogen) to amplify the 213-bp fragment from 10 ng DNA derived from stool samples from the ileostomy or the pouch within 50 days after stoma closure with 16S rRNA gene primers 27F (5′-AGAGTTTGATCCTGGCTCAG-3′) and 1492R (5′-GGTTACCTTGTTACGACTT-3′) (the same as the primers used in the previous T-RFLP analysis) [2]. DNA was initially denatured at 94 °C for 2 min, and then passed through 37 cycles of 94 °C for 30 s, 50 °C for 30 s, and 68 °C for 90 s. Amplification products were purified using Wizard PCR Preps DNA purification system (Promega Co., Tokyo, Japan) and digested with *Cfo* I (Roche Diagnostics Co.), an isozyme of *Hha* I that yielded in the 213-bp ileal fragment in the previous report. Digested DNA was then electrophoresed on a 6 % acrylamide gel and visualized using SYBR Green I (FMC, Rockland, USA). Gel sections corresponding to fragments that span the 213-bp-size region of the gel were visualized with UV and excised. DNA was recovered from the gel, precipitated with ethanol, and self-ligated using DNA ligase (Roche Diagnostics Co.). Subsequent product (equivalent to 1 μl of the original PCR reaction) was used as a template and re-amplified using only the 27F primer through 37 cycles of 94 °C for 20 s, 60 °C for 20 s, and 68 °C for 20 s with a final extension period at 68 °C for 5 min. The resulting amplification products (before and after *Cfo* I digestion) were resolved by polyacrylamide electrophoresis, cloned and sequenced; the resulting sequence served as the probe for DNA homology searches within the BLAST network service (http://blast.ncbi.nlm.nih.gov/Blast.cgi).

Statistical Analysis

Relative copy number values estimated with real-time PCR are presented as median and percentile values within each

group. A Kruskal-Wallis rank test was used to determine if there was a significant correlation among the six sample groups. A Mann–Whitney test was used to compare two independent groups. A Wilcoxon signed-ranks test was used to compare paired groups, with significance at $p < 0.01$.

Results

Recovery of Fecal DNA

Adequate quantity and quality of DNA samples were obtained from both firm and watery stool samples (Fig. 1). Median concentrations of sample DNA included 2.3 μg/g stool in the ileostomy group, 7.7 μg/g in patients with an ileal pouch within 50 days of ileostomy closure, 11.9 μg/g from 50 to 100 days, 13.3 μg/g from 100 days to 1 year, and 12.4 μg/g in patients with an established ileal pouch (more than 1 year since ileostomy closure). In contrast, DNA concentrations from control group samples averaged 42.9 μg/g. Because the amount of DNA recovered per gram of wet stool varied and was not necessarily proportional to stool weight, we estimated DNA copy number (number of 16S rRNA genes per μg stool DNA) median and range from the 25th and 75th percentile values within each group. Control plasmids for real-time PCR were obtained by amplification of bacterial 16S rRNA genes with the primer pairs listed in Table 2, followed by cloning of the resulting fragments into plasmid vectors and verification of sequence (data not shown).

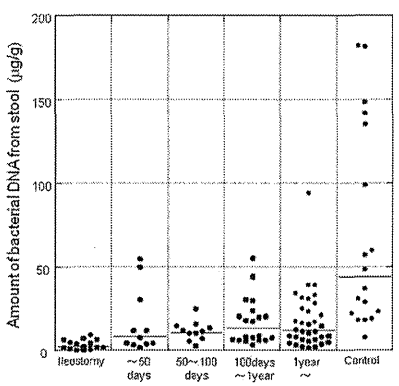

Fig. 1 DNA recovery from stool samples (μg DNA per gram wet stools) in the six study groups

Time-Dependent Changes in 16S rRNA Gene Copy Number in Feces

In preliminary experiments, we estimated 16S rRNA gene copy number from stool samples obtained from two patients (A and B) at various time intervals since ileostomy closure (Fig. 2). While the total amount of all eubacteria (expressed by 16S rRNA gene copy number per μg stool DNA) was stable, changes in the relative copy numbers of different bacteria were observed within 2–3 months after ileostomy closure. Early changes included an increase in *Atopobium*, *C. coccoiodes*, and *Bifidobacterium* in patient A, and an increase in *C. coccoides*, *B. fragilis*, and *Bifidobacterium* in patient B. The amount of DNA detected for each strain correlated positively with the number of days since ileostomy closure. We observed the greatest change within approximately 50 days, less change between 50 and 100 days, and almost no change between 100 days and 1 year. Based on these preliminary results, we classified pouch samples in the larger group study into four groups based on the time since ileostomy closure (<50, 50–100 days, 100 days–1 year, >1 year).

Significant changes in relative copy number over time (using a Kruskal-Wallis rank test) were detected in the *C. coccides* group, *C. leptum* subgroup, *B. fragilis* group, *Atopobium* cluster, *Lactobacillus* species, and not in *Bifidobacterium*, *Prevotella*, and *Desulfovibrios* (Fig. 3, Table 3). Anaerobic bacteria in the *C. coccoides* group, *C. leptum* subgroup, *B. fragilis* group, and *Atopobium* cluster were less abundant in samples just after ileostomy closure and showed a time-dependent increase in copy number; however, even in pouches more than 1 year old, the levels of these anaerobes never exceeded those from healthy controls. Levels of specific bacteria, particularly *C. coccoides* and *B. fragilis* groups, were more consistent in control group samples than in post-surgical samples. In contrast, the quantity of *Lactobacillus* species was most abundant in ileostomy samples and then decreased after ilesotomy closure to levels comparable to controls. We found no significant difference in bacteria levels between samples from pouches at 1 year after ileostomy closure and those after an additional year (Table 4).

Identification and Quantification of the 213-bp "Ileal" Fragment

In a previous study, we detected a 213-bp PCR fragment preferentially in samples taken at the time of ileostomy and from early-stage pouches [2]. In this study, we PCR-amplified 213-bp fragments of DNA from one patient's stool samples taken at the time of ileostomy closure (Fig. 4a, lane 1), and 14 days after ileostomy closure (Lane 2). We used electroelution to recover these fragments and then

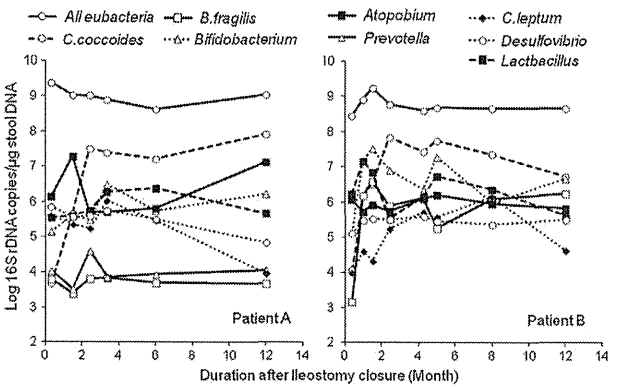

Fig. 2 Progressive changes in copy numbers of fecal bacteria species and groups measured at increasing time points since the time of ileostomy closure in two patients (*A* and *B*). *Plotted points* mark the logarithmic number of 16S rRNA gene copies per μg stool DNA relative to the number of months since ileostomy closure

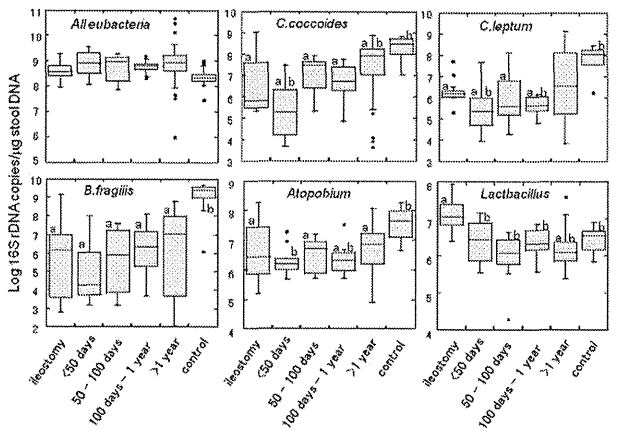

Fig. 3 Estimated logarithmic number of 16S rRNA gene copies per μg stool DNA. The copy number of fecal bacteria types in stool samples from ileostomies, pouches within 50 days of closure, pouches from 50 to 100 days, pouches from 100 days to 1 year, pouches over 1 year after ileostomy closure, and controls are illustrated. *Shaded bars* and *lines* represent 25/75 % percentile and median values, respectively. *Error bars* indicate 10/90 % percentile values. *p*-values were calculated by Kruskal–Wallis rank test, with significance at $p < 0.01$. *a* and *b* indicate a statistically significant difference ($p < 0.01$ by Mann–Whitney-Wilcoxon test) in the copy number of samples relative to the control (*a*) or ileostomy group (*b*), respectively

self-ligated them for use as template in further amplifications. Among the products re-amplified with only the 27F primer, bands of approximately 430-bp were detected in both samples (Fig. 4b). Similarly, PCR amplified products from both templates yielded two restriction fragments (approximately 200- and 220-bp long) when digested with *Cfo I* (Fig. 4c). Among the 11 plasmid clones recovered with these DNA fragments, insert sizes were 107, 192, 202, 218, and 238 bp, respectively. The 218-bp DNA fragment encoded a *Cfo I* restriction site at its 3′-end and its sequence was strictly homologous to a partial sequence of the *Enterococcus faecalis* 16S ribosomal RNA gene (AB530699.1 etc.).

Upon identifying the origin of the 213-bp fragment, we measured the amount of *Enterococcus* species and *Enterococcus faecalis* using specific16S ribosomal RNA gene primers (Fig. 5), and found that *Enterococcus* species and *Enterococcus faecalis* were most abundant in samples from pouches within 50 days after ileostomy closure, and least abundant in the control group. When we compared levels of *Enterococcal* bacteria between samples from

Table 3 Changes in relative number over time

Bacterial group	Ileostomy	<50 days	50–100 days	100 days–1 year	>1 year	Healthy volunteer	*p*-value
Bifidbacterium	7.08	6.22	5.91	6.43	6.49	6.60	$p = 0.0785$
	6.26/7.83	5.16/7.11	5.72/6.20	5.99/6.74	5.73/7.24	6.00/8.26	
Prevotella	4.57	3.96[a]	3.86	3.90	4.55[b]	4.42	$p = 0.3971$
	3.93/5.81	3.58/4.91	3.67/5.10	3.64/4.28	3.78/5.55	4.03/4.86	
Desulfovibrios	5.64	5.53	5.50	5.61	5.61	5.80	$p = 0.3131$
	5.58/5.81	5.41/4.91	5.49/5.62	5.49/5.72	5.42/5.73	5.65/6.01	

Values are the median logarithmic number of rDNA copies per µg stool DNA, and 25/75 % percentile values. Samples yielding values below the sensitivity threshold were excluded from the statistical analysis ([a] 2 samples, [b] 14 samples excluded). *p*-values were calculated by Kruskal–Wallis rank test

Table 4 Bacteria levels long after ileostomy closure

Bacterial group	Time point over 1 year	Time point plus an additional 1 year	*p*-value
All Eubacteria	9.15	8.86	$p = 0.1094$
	10.34/8.62	8.65/9.05	
C. coccoides	8.23	8.07	$p = 0.4375$
	8.88/6.71	7.99/8.15	
B. fragilis	6.87	7.69	$p = 0.5781$
	8.04/5.60	6.66/8.25	
Bifidobacterium	7.02	7.01	$p = 0.6875$
	7.84/5.41	6.52/7.50	
Lactobacillus	6.20	6.06	$p = 0.6721$
	6.52/5.86	5.94/6.24	
Atopobium	6.75	7.11	$p = 0.4687$
	7.45/6.00	6.23/7.61	
Prevotella	5.12	5.37	$p = 0.375$
	5.88/4.50	4.96/5.71	
C. leptum	8.17	7.18	$p = 0.2188$
	9.15/6.21	6.37/8.37	
Desulfovibrio	5.86	5.58	$p = 0.9489$
	8.61/4.61	5.24/5.73	

Values are the median logarithmic number of rDNA copies per µg stool DNA, and 25/75 % percentile values. *p*-values were calculated by Wilcoxon signed-ranks test

pouches of various times since closure, we found that there were fewer of these bacteria as the time since ileostomy closure increased. In addition, there was a significantly higher frequency of fecal samples with low-detectability levels of *Enterococcus faecalis* among patients 1 year after ileostomy closure relative to control subjects. These findings suggest that *Enterococcus* species predominate transiently during the first 50 days of post-surgical adaptation.

Discussion

The human gastrointestinal tract is postulated to harbor a complex community of over 10^{14} microorganisms. This community has the power to influence gut physiology and health via a number of activities, including fermentation of dietary components, production of short-chain fatty acids, modulation of the immune system, transformation of bile acids, production of vitamins and health-protective substances, and provision of a barrier against pathogenic bacteria [11]. Gut flora also affects host immunity and may be an important contributor to altered immune responses after total proctocolectomy.

Pouchitis is a non-specific mucosal inflammation in a pouch. It has been suggested to be the most frequent complication with a pelvic pouch, as well as with a Kock continent ileostomy at late stage [12]. The fact that antibiotics, including metronidazole and ciprofloxacin, are effective in treating pouchitis indicates a direct or indirect link of pouch microbiota to this mucosal inflammation with unknown etiology. Floral changes in the ileal pouch may

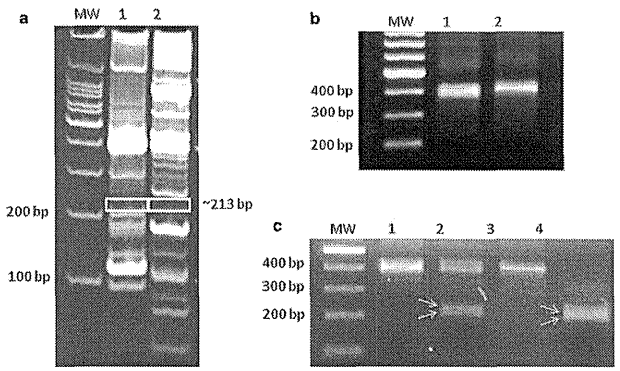

Fig. 4 **a** Gel electrophoresis of PCR-amplified samples using the universal 16S rDNA primers. *Lane 1*: ileostomy sample, *Lane 2*: pouch sample 14 days after ileostomy closure. *White rectangles* mark boundaries of the gel slab that was excised for DNA extraction. **b** Extracted DNAs from (**a**) were self-ligated, PCR-amplified with only the 27F primer of the universal 16S rDNA primer set, and resolved by gel electrophoresis. *Lane 1*: ileostomy sample; *Lane 2*: a sample from the pouch at 14 days after ileostomy closure. **c** Gel electrophoresis before (*Lanes 1, 3*) and after (*Lanes 2, 4*) treatment of PCR products in (**b**) with *Cfo* I. *Lanes 1* and 2: ileostomy sample; *Lanes 3* and *4*: sample from the pouch at 14 days after ileostomy closure. *Arrows* indicate two molecules with slightly different mobilities

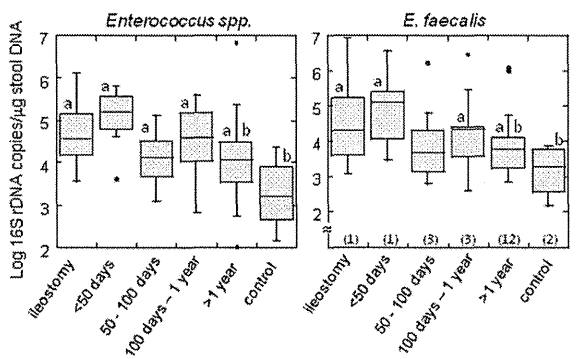

Fig. 5 Estimated copy number of the 16S rDNA gene from *Enterococcus* species (*left panel*) and *E. faecalis* (*right panel*) in samples from ileostomies, pouches within 50 days, pouches from 50 to 100 days, pouches from 100 days to 1 year, pouches over 1 year after ileostomy closure, and control stool samples. The *y*-axis represents the logarithmic number of 16S rDNA copies per µg stool DNA. *Shaded bars* and lines represent 25/75 % percentile and median values, respectively. *Error bars* indicate 10/90 % percentile values. *p*-values were calculated by Kruskal–Wallis rank test, with significance at $p < 0.01$. *a* and *b* indicate a statistically significant difference ($p < 0.01$ by Mann–Whitney-Wilcoxon test) in the copy number of samples relative to the control (*a*) or ileostomy group (*b*), respectively. For *E. faecalis* data, the number with a parenthesis at the bottom of the chart mark indicate the number of samples that yielded DNA levels below the threshold sensitivity and were not analyzed

be associated with triggering and/or amplifying mucosal inflammation of the pouch. For these reasons, evaluation of the pouch flora is essential.

Since the water content in stool after total proctocolectomy is generally very high and easily affected by meals or enteritis, DNA recovery per gram wet stool is highly

variable and not necessarily proportional to wet weight of stool samples. Therefore, we compared flora density and diversity using real-time-PCR of 16S rRNA genes to estimate the numbers of bacteria present per microgram stool DNA. Data from this study expand our understanding of the time-dependent progression in fecal flora (from "ileal" to "colonic") after ileostomy closure [2] by providing explicit values for specific species, genera, group, or subgroup densities in samples collected at various times since ileostomy closure. Overall, we found increased numbers of colon-predominant anaerobic bacteriae and decreased numbers of ileum-predominant species. In addition, the relative numbers of these bacteria were observed to stabilize within 1 year after ileostomy closure.

Using conventional culture techniques, Nasmyth et al. compared fecal flora from 11 pouches and 12 ileostomies and found a significant increase in numbers of anaerobic bacteria (such as *Bacteroides* and *Bifidobacteria*) in pouch-derived samples [13]. Smith et al. also investigated individual strains of fecal anaerobic bacteria in seven ileostomies, nine ileal pouches with UC, and five ileal pouches with FAP using conventional culture methods [14] and found that the ratio of strict to facultative anaerobes within the UC pouch was maintained between sample groups. In this study, we investigated changes in common fecal bacteria using molecular techniques that permit analyses of bacterial DNAs extracted from both cultivable and uncultivable bacteria. Molecular data demonstrate a similar increase in anaerobic bacteria such as *C. coccides* group, *C. leptum* subgroup, *B. fragilis* group, and *Atopobium* cluster with time. Although our methods detected major populations of fecal bacteria, it is certainly possible that low-abundance taxa not detected using quantitative PCR may also contribute significantly to changes in microbial population structures following total proctocolectomy.

There are several possible limitations to the methodologies used in this study. First, efficiencies of DNA extraction in gram-positive versus -negative bacteria can differ due to different cell-wall components. Second, DNAs from living bacteria and dead bacteria that are sufficiently intact for amplification will both yield amplication products. Finally, the fact that patients typically receive antibiotics until the fourth post-operative day must be taken into consideration in that this may bias the bacterial composition of ileostomy samples. Despite these limitations, results from conventional culture and molecular studies are similar and indicate that increased numbers of anaerobic bacteria are highly relevant in pouches after total proctocolectomy, and that quantification of fecal bacteria using real-time PCR is appropriate and useful.

Although the mechanism for altering bacterial composition during intestinal adaptation is speculative, a "colonic transformation" includes both of the acquisition of colonic flora phenotypes as well as the loss of small intestinal phenotypes after total proctocolectomy. Postoperative changes in the host include activation of the renninangiotensin-aldosterone system, altered phenotype of the remnant small intestine epithelia, stasis due to pouch formation, and possible alterations in mucosal immune response [1, 15]. Consistent with the concept of "colonic transformation," we observed that the abundance of *Lactobacillus* and *Enterococcus* species that predominate in the small intestine decreases progressively after ileostomy closure.

The changes that occur during intestinal adaptation also depend on other variables that affect bacterial composition after total proctocolectomy, including original flora before surgery, meal components, hygiene environment, and genetic background of the host. In order to study variation in fecal flora, repeated sampling from the same individuals over a course of time is necessary. We measured bacteria in feces because it is feasible to collect repeated samples from both healthy individuals and patients. While both mucosa-associated microbiota and those attached to epithelial cells may also have a strong impact on gut physiology and pathology after total proctocolectomy [16–18], previous DNA-based approaches have reported a similarity index of approximately 85 % between fecal microbiota and mucosa-associated microbiota [19], suggesting that analysis of fecal bacteria is a relevant measure. Regardless of the variation that is observed in the bacterial composition of feces between individuals, increased numbers of anaerobic bacteria and decreased numbers of small-intestine bacteria appear to be consistent and relevant postoperative phenomena following total proctocolectomy.

In a previous study, an approximately 213-bp terminal restriction fragment was detected in more than 70 % of ileostomy samples, a significantly greater frequency ($p < 0.05$) than in controls [2]. Because this predominantly "ileal" fragment exhibited time-dependent decreases in detection after ileostomy closure, we hypothesized decreased numbers of "ileal" bacteria and increased numbers of "colonic" bacteria were hallmarks of the mucosal immune response after ileostomy closure. In this study, we continued our analysis by successfully cloning a 218-bp fragment with sequence identical to a partial sequence of the *Enterococcus faecalis* 16S ribosomal RNA gene. With only a five base-pair difference between the expected and identified fragments, and since *Enterococcus faecalis* decreased in a time-dependent fashion after ileostomy closure, we considered the 218-bp fragment to be our target. The five-base misreads in the previous T-RFLP study might have led to our previous failure in hitting in the database.

Inflammation of the ileal pouch, or "pouchitis," has been hypothesized to be linked with the presence of large numbers of sulfate-reducing bacteria of the genus

Desulfovibrio in stools [5]. Sulfide, a product of sulfate reduction, has been shown to inhibit butyrate metabolism in colonocytes and to induce epithelial abnormalities such as hyperproliferation [20]. In a comparison of cultures of sulfate-reducing bacteria derived from UC pouches versus familial adenomatous polyposis (FAP) pouches, Duffys et al. found sulfate-reducing bacteria in 80 % of UC pouches, but none in FAP pouches [21]. In the present study, we found that the amount of *Desufovibrios* throughout the postoperative term was both stable and comparable to that of control cases. Although samples in this study were all obtained from pouches without inflammation, it is essential to monitor *Desulfovibrios* levels before and after therapies when patients are at risk for pouchitis. In future analyses, samples from patients with familial adenomatous polyposis could provide additional information about pouchitis development.

In conclusion, our molecular quantification of fecal bacteria clearly demonstrates a time-dependent shift in fecal flora from ileal to colonic bacteria after total proctocolectomy. Although the study is still descriptive, postoperative alteration of fecal flora will be one essential element in future investigations of pouchitis development.

Acknowledgments A part of the results were generated by using the facilities of the Biomedical Research Core of Tohoku University Graduate School of Medicine. This work was supported in part by Health and Labour Sciences Research Grants for research on intractable diseases from the Ministry of Health, Labour and Welfare of Japan.

Conflict of interest The authors declare that they have no conflict of interest.

References

1. Fukushima K, Haneda S, Takahashi K, et al. Molecular analysis of colonic transformation in the ileum after total colectomy in rats. *Surgery*. 2006;140:93–99.
2. Kohyama A, Ogawa H, Funayama Y, et al. Bacterial population moves toward a colon-like community in the pouch after total proctocolectomy. *Surgery*. 2009;145:435–447.
3. Matsuki T, Watanabe K, Fujimoto J, Takada T, Tanaka R. Use of 16S rRNA gene-targeted group-specific primers for real-time PCR analysis of predominant bacteria in human feces. *Appl Environ Microbiol*. 2004;70:7220–7228.
4. Rinttila T, Kassinen A, Malinen E, Krogius L, Palva A. Development of an extensive set of 16S rDNA-targeted primers for quantification of pathogenic and indigenous bacteria in faecal samples by real-time PCR. *J Appl Microbiol*. 2004;97:1166–1177.
5. Ohge H, Furne JK, Springfield J, Rothenberger DA, Madoff RD, Levitt MD. Association between fecal hydrogen sulfide production and pouchitis. *Dis Colon Rectum*. 2005;48:469–475.
6. Roediger WE, Duncan A, Kapaniris O, Millard S. Sulphide impairment of substrate oxidation in rat colonocytes: a biochemical basis for ulcerative colitis? *Clin Sci Lond*. 1993;85:623–627.
7. Nadkarni MA, Martin FE, Jacques NA, Hunter N. Determination of bacterial load by real-time PCR using a broad-range (universal) probe and primers set. *Microbiology*. 2002;148:257–266.
8. Fite A, Macfarlane GT, Cummings JH, et al. Identification and quantitation of mucosal and faecal desulfovibrios using real time polymerase chain reaction. *Gut*. 2004;53:523–529.
9. Menard JP, Fenollar F, Henry M, Bretelle F, Raoult D. Molecular quantification of Gardnerella vaginalis and Atopobium vaginae loads to predict bacterial vaginosis. *Clin Infect Dis*. 2008;47:33–43.
10. Bartosch S, Fite A, Macfarlane GT, McMurdo ME. Characterization of bacterial communities in feces from healthy elderly volunteers and hospitalized elderly patients by using real-time PCR and effects of antibiotic treatment on the fecal microbiota. *Appl Environ Microbiol*. 2004;70:3575–3581.
11. Langendijk PS, Schut F, Jansen GJ, et al. Quantitative fluorescence in situ hybridization of Bifidobacterium spp. with genus-specific 16S rRNA-targeted probes and its application in fecal samples. *Appl Environ Microbiol*. 1995;61:3069–3075.
12. Coffey JC, Rowan F, Burke J, Dochery NG, Kirwan WO, O'Connell PR. Pathogenesis of and unifying hypothesis for idiopathic pouchitis. *Am J Gastroenterol*. 2009;104:1013–1023.
13. Nasmyth DG, Godwin PG, Dixon MF, Williams NS, Johnston D. Ileal ecology after pouch-anal anastomosis or ileostomy. A study of mucosal morphology, fecal bacteriology, fecal volatile fatty acids, and their interrelationship. *Gastroenterology*. 1989;96:817–824.
14. Smith FM, Coffey JC, Kell MR, O'Sullivan M, Redmond HP, Kirwan WO. A characterization of anaerobic colonization and associated mucosal adaptations in the undiseased ileal pouch. *Colorectal Dis*. 2005;7:563–570.
15. Sato S, Fukushima K, Naito H, et al. Induction of 11beta-hydroxysteroid dehydrogenase type 2 and hyperaldosteronism are essential for enhanced sodium absorption after total colectomy in rats. *Surgery*. 2005;137:75–84.
16. Swidsinski A, Ladhoff A, Pernthaler A, et al. Mucosal flora in inflammatory bowel disease. *Gastroenterology*. 2002;122:44–54.
17. Marteau P, Lepage P, Mangin I, et al. Review article: gut flora and inflammatory bowel disease. *Aliment Pharmacol Ther*. 2004;20:18–23.
18. Lepage P, Seksik P, Sutren M, et al. Biodiversity of the mucosa-associated microbiota is stable along the distal digestive tract in healthy individuals and patients with IBD. *Inflamm Bowel Dis*. 2005;11:473–480.
19. Sokol H, Seksik P, Rigottier-Gois L, et al. Specificities of the fecal microbiota in inflammatory bowel disease. *Inflamm Bowel Dis*. 2006;12:106–111.
20. Christl SU, Eisner HD, Dusel G, Kasper H, Scheppach W. Antagonistic effects of sulfide and butyrate on proliferation of colonic mucosa: a potential role for these agents in the pathogenesis of ulcerative colitis. *Dig Dis Sci*. 1996;41:2477–2481.
21. Duffy M, O'Mahony L, Coffey JC, et al. Sulfate-reducing bacteria colonize pouches formed for ulcerative colitis but not for familial adenomatous polyposis. *Dis Colon Rectum*. 2002;45:384–388.

Int. J. Oral Maxillofac. Surg. 2012; 41: 1161–1169
http://dx.doi.org/10.1016/j.ijom.2012.05.020, available online at http://www.sciencedirect.com

International Journal of
Oral & Maxillofacial Surgery

Research Paper
Bone Regeneration

Octacalcium phosphate collagen composites with titanium mesh facilitate alveolar augmentation in canine mandibular bone defects

K. Miura[1], K. Matsui[2], T. Kawai[2], Y. Kato[2], A. Matsui[2], O. Suzuki[3], S. Kamakura[4], S. Echigo[2]

[1]Department of Regenerative Oral Surgery, Unit of Translational Medicine, Graduate School of Biomedical Sciences, Nagasaki University, Japan; [2]Division of Oral Surgery, Department of Oral Medicine and Surgery, Tohoku University Graduate School of Dentistry, Japan; [3]Division of Craniofacial Function Engineering, Tohoku University Graduate School of Dentistry, Japan; [4]Bone Regenerative Engineering Laboratory, Graduate School of Biomedical Engineering, Tohoku University, Japan

K. Miura, K. Matsui, T. Kawai, Y. Kato, A. Matsui, O. Suzuki, S. Kamakura, S. Echigo: Octacalcium phosphate collagen composites with titanium mesh facilitate alveolar augmentation in canine mandibular bone defects. Int. J. Oral Maxillofac. Surg. 2012; 41: 1161–1169.

Abstract. This study was designed to investigate whether bone regeneration by implantation of octacalcium phosphate and porcine atelocollagen composite (OCP/Col) would be enhanced if mechanical stress to the implanted OCP/Col were alleviated. OCP/Col discs were implanted into an arc-shaped mandibular defect in male adult beagle dogs divided into untreated, OCP/Col, and OCP/Col/Mesh groups. In the OCP/Col/Mesh group, mechanical stress towards the implanted OCP/Col was alleviated by a titanium mesh. Bone regeneration in the three groups was compared after 6 months. Macroscopically, the alveolus in the OCP/Col/Mesh group was augmented vertically more than in the other two groups. Morphometric analysis by micro-CT showed the bone volume in the OCP/Col/Mesh group was significantly greater than in the other two groups. The augmented alveolus in the OCP/Col/Mesh group consisted of outer cortical and inner cancellous structure. Histologically, the OCP/Col/Mesh-treated alveolus was augmented by matured bone tissue along the inside of the titanium mesh. The implanted OCP/Col in the OCP/Col/Mesh and OCP/Col groups had almost disappeared. These results indicated that vertical bone regeneration by OCP/Col was efficient and successful when the mechanical stress to the implanted OCP/Col was alleviated. OCP/Col should be a useful bone substitute with active structural reconstitution.

Keywords: bone regeneration; octacalcium phosphate; mechanical stress; titanium mesh; dog.

Accepted for publication 16 May 2012
Available online 22 June 2012

Achieving bone regeneration for bone defects is a crucial issue in oral and orthopaedic surgery.[1] Many cases require bone regeneration, for example, reconstruction of bone defect after extirpation of jaw tumours and cysts, bone grafting for alveolar cleft,[2] and preprosthetic surgery of sinus lifting for bone deficiency.[3] Autogenous iliac bone grafting is the most popular bone regenerative technique for large bone defects that cannot be expected to exhibit self-restoration.[2] This technique has several drawbacks, such as limited quantity of harvested bone and excessive surgical intervention into healthy tissue,[4] as well as low availability for general dental practitioners. Therefore, many bone substitutes have been developed as alternatives to autogenous bone grafting, and hydroxyapatite (HA) and β-tricalcium phosphate (β-TCP) have been applied in clinical contexts.[4,5] Autogenous bone grafting is still the gold standard because HA and β-TCP did not accomplish bone regeneration, in contrast to autogenous bone grafting.

Interstitial bone material consists of organic matrices, such as collagen, and minerals whose prototype is considered to be HA. Octacalcium phosphate ($Ca_8H_2(PO_4)_6{\cdot}5H_2O$; OCP) is considered to be a direct precursor of HA,[6] and the transition of OCP to HA is likely to be spontaneous and irreversible under physiological conditions.[6] The osteoconductive property of synthetic granular OCP was first seen in the subperiosteal implantation of mouse calvaria, and the implanted OCP was converted to the apatitic phase.[7] As OCP was capable of inducing osteoblastic cell differentiation in a manner comparable to HA,[8] the implanted granules of OCP are resorbed and replaced by newly formed bone to a greater extent than those of β-TCP and HA.[9]

Even though OCP possesses many desirable properties as a bone substitute, it cannot be moulded using sintering processes, unlike bioceramics such as HA or β-TCP, because of its intrinsic crystal structure.[6] When considering clinical use, it is easy to assume the limited availability of granular OCP as well as that of granular HA or β-TCP. To resolve these disadvantages, a composite sponge constructed of synthetic OCP and porcine atelocollagen (OCP/Col) was developed.[10] The authors' previous studies reported that OCP/Col significantly enhanced bone regeneration more than the implantation of OCP alone, β-TCP collagen composite (β-TCP/Col), or HA collagen composite (HA/Col), if implanted into a critical-sized calvarial defect rat model.[10,11] The efficacy of bone regeneration by OCP/Col was confirmed in various canine bone defect models.[12–14]

It has been accepted that the three main components for bone regeneration are stem cells or osteoprogenitors, an appropriate biological scaffold, and signal molecules,[15] and the importance of mechanical stress in bone regeneration has been advocated.[16] Bone is a dynamic tissue that constantly undergoes remodelling even once growth and modelling of the skeleton have been completed, and the cells responsible for bone remodelling are known as osteocytes, osteoblasts, and osteoclasts. Osteocytes have the ability to communicate with osteoblasts through an extensive network of cellular processes, and this network is thought to sense and respond to local mechanical stress.[16]

Although implantation of OCP/Col showed prominent bone regenerative properties at a site with minimal stress, limited bone regeneration with stimulation of osteoclastic resorption was demonstrated at mechanically stressed bone defects.[17] The bone regeneration by OCP/Col would be recovered if the mechanical stress were alleviated by the use of support material.[18] It has been reported that the alveolar defects of adult dog were augmented when a micro-titanium mesh was used to alleviate mechanical stress.[10] The present study was designed to investigate whether bone regeneration by implantation of OCP/Col would be enhanced if mechanical stress to the implant were alleviated. With the goal of clinical use, a critical-sized mandibular defect was prepared for an adult dog, and discs of OCP/Col with titanium mesh that alleviates mechanical stress were implanted into the defect. After 6 months of implantation, bone regeneration by OCP/Col with and without titanium mesh was compared.

Materials and methods

Preparation of OCP and OCP/Col discs

Preparation of the discs of OCP and OCP/Col has been described previously.[10,20] Briefly, OCP was prepared by direct precipitation,[7] and collagen was prepared from NMP collagen PS (Nippon Meat Packers, Tsukuba, Ibaraki, Japan), a lyophilized powder of pepsin-digested atelocollagen isolated from porcine dermis. The sieved granules (particle size 300–500 μm) of OCP were added to the concentrated collagen and mixed, and the weight percentage of OCP in OCP/Col became 77%. The OCP/Col mixture was lyophilized, and the disc was moulded (9 mm diameter, 1 mm thick). The moulded OCP/Col underwent dehydrothermal treatment (150 °C, 24 h) in a vacuum drying oven and was then sterilized using gamma-ray irradiation (5 kGy). Under standardized conditions (60 kV, 10 mA, 11 s), the OCP/Col discs before implantation showed no radiopacity.

Animals and implantation procedures

17-Month-old, male beagle dogs ($n = 9$; NARC Co., Chiba, Japan) were used. The principles of laboratory animal care were followed as well as national laws, and all procedures were approved by the Animal Research Committee of Tohoku University (21-Dentistry Animal-23).

General anaesthesia was administered with intravenous sodium pentobarbital (0.5 ml/kg), followed by intramuscular atropine sulfate (0.5 mg) and ketamine hydrochloride (20 mg/kg). After disinfection of the oral cavity, local anaesthesia (2% lidocaine with 1/80,000 epinephrine) was injected. The preparation of left mandibular defect was as follows: at first, left lower second and third premolars were extracted and a buccal intracrevicular incision was made from the centre of the first premolar to the fourth premolar. A vertical incision was made from the marginal gingiva of the fourth premolar towards the inferior border of the mandible, and the mucoperiosteum of the first to fourth premolars of the mandible was ablated in circumference. An arc-shaped defect (about 10 mm radius) was made from the interalveolar septum of the first and second to the third and fourth premolars. The middle point of 20 mm of the alveolar crest between the extracted second and third premolars was point M. The point 10 mm away from point M, which was on a perpendicular line vertically towards the mandibular border from point M was defined the bottom of the defect (Figs. 1a and 2a). After preparation of the defect, radiographs were taken to ensure that there were no remaining teeth in the defect, and the mucoperiosteal flap was advanced to cover the defect.

The experimental animals were divided into three groups, and each group included three samples. Group 1 was untreated (Figs. 1a and 2a); nothing was implanted into the prepared mandibular defect. Group 2 was the OCP/Col group (Figs. 1b and 2b); as many OCP/Col discs as possible were implanted into the prepared mandibular defect, the average was 14.7. Group 3 was the OCP/Col/Mesh group (Figs. 1c and 2c); the remaining mandible was surrounded by titanium mesh (0.1 mm thick, hole spacing 0.75 mm × 1.3 mm, Flexgitter 1.0; Synthes®, Tokyo, Japan) to alleviate mechanical stress on the implants, and the mesh was fixed to the mandible using two titanium mini-screws, as many OCP/Col discs as possible were implanted into the prepared mandibular defect, the average was 12.7. Finally, all of the experimental defects were closed watertight (Fig. 2d).

0901-5027/0901161 + 09 $36.00/0

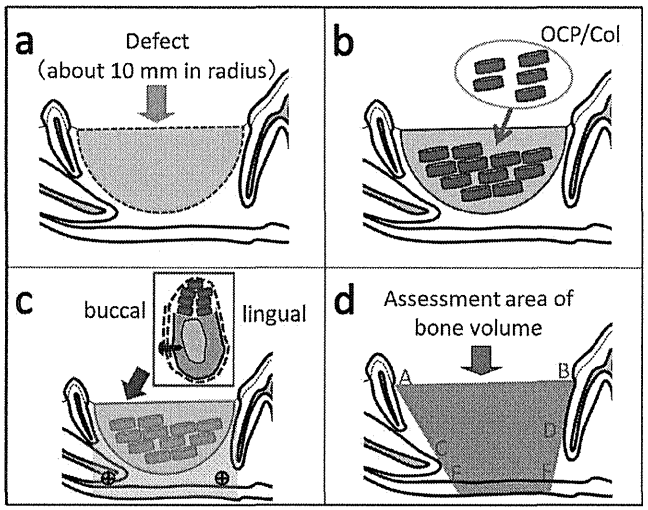

Fig. 1. The preparation and implantation procedures for the left mandibular defect (a–c) and the measurement of bone volume in the defect (d). The left lower second and third premolars are extracted, and the arc-shaped defect (about 10 mm radius) is made (a). The discs of OCP/Col are implanted into the defect in the OCP/Col group (b). In the OCP/Col/Mesh group, disks of OCP/Col with surrounding titanium mesh that alleviates mechanical stress to the disks are implanted into the defect (c). The measurement of bone volume in the defect and the area of interest are defined as follows: the upper border is a line from the distal cement–enamel junction of the first premolar (A) to the mesial cement–enamel junction of the fourth premolar (B). The lower border is the inferior mandibular border. The mesial border is the line from A through the root apex of the canine tooth (C) towards the inferior mandibular border, and the intersection is defined as E. The distal border is the tangential line from B through the mesial root border of the fourth premolar (D) towards the inferior mandibular border, and the intersection is defined as F. An area enclosed by A, E, F, and B is defined as the area of interest, then the bone volume is obtained by integrating the area of interest from the buccal to the lingual side (d).

To prevent infection, flomoxef sodium was used via an intravenous drip during the operation, and cefcapene pivoxil hydrochloride hydrate was administered orally for 3 days postsurgically. A soft diet was fed to rest the operative wounds during the experimental period.

Tissue preparation and radiography

Dental radiographs were taken by dental radiography (SANKO X-ray MFG or MAX-DC70) with instant film for occlusal radiography (Hanshin Technical Laboratory, Ltd., Nishinomiya, Hyogo, Japan) under standardized conditions (50 kV, 10 mA, 0.8–1.0 s or 60 kV, 10 mA, 0.1 s) immediately after the operation and every month thereafter to confirm the condition of the treated defect. 6 months after implant surgery, the dogs were killed by intravenous injection of an overdose of sodium pentobarbital. The mandible and surrounding tissues were resected and fixed with 10% formalin neutral buffer solution, pH 7.4.

Micro-CT examination

The morphological and quantitative image analysis of newly formed bone was performed using micro-computed tomography (CT) (Scan Xmate-E090; Comscantecno Co., Ltd., Kanagawa, Japan) under standardized conditions (90 kV, 110 μA). In the three-dimensional analysis, the newly formed bone area was analyzed after sampling using bone mineral density (BMD) standards, established as over 300 mg/cm^3 (between 300 mg/cm^3 and 1500 mg/cm^3), and the extracted range of bone was defined between 300 mg/cm^3 and 1100 mg/cm^3.

An area of interest was defined and the bone volume in the area of interest was quantified as follows (Fig. 1d). The upper border defined as a curved surface was the line from the distal cement–enamel junction of the first premolar (A) to the mesial cement–enamel junction of the fourth premolar (B). The lower border was defined as the inferior mandibular border. The mesial border defined as a curved surface was the line from A through the root apex of the canine tooth (C) towards the inferior mandibular border, and the intersection was defined as E. The distal border was the tangential line from B through the mesial root border of the fourth premolar (D) towards the inferior mandibular border, and the intersection was defined as F. An area enclosed by A, E, F, and B was defined as the area of interest, then the bone volume was obtained by integrating the area of interest from the buccal to the lingual side. The bone volume in the operated site was measured using a morphometric programme of TRI/three-dimensional BON (Ratoc System Engineering, Osaka, Japan).[21] The height and width of the treated mandible were measured and

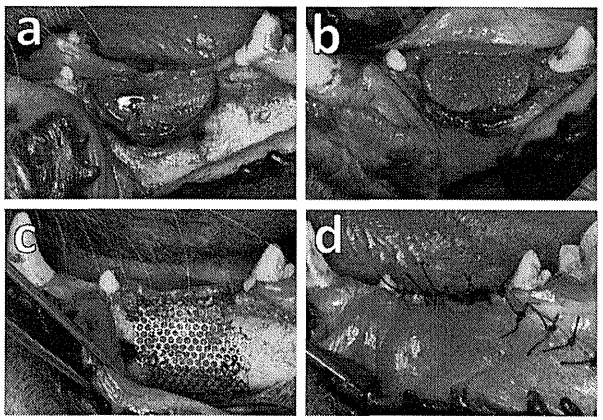

Fig. 2. Macroscopic view of the prepared mandibular defect and implantation procedures. The arc-shaped defect is made, and the bottom of the created defect is situated about 10 mm from the alveolar crest (a). The disks of OCP/Col are implanted into the defect in the OCP/Col group (b). In the OCP/Col/Mesh group, disks of OCP/Col with titanium mesh are implanted into the defect (c). All the experimental defects are closed watertight (d).

statistically analyzed. The measured plane was the frontal plane at the centre between A and B, which was vertical to the inferior border of the mandibular.

Statistical analysis

Statistical analysis was performed for all of the micro-CT data using Excel v.X. (Microsoft Co., Redmond, WA, USA). All values are reported as the means ± standard error (SE). The χ^2 test was applied to test whether each group had a normal distribution, and Bartlett's test was used to examine for homogeneity of variances across samples. One-way analysis of variance (ANOVA) or the Kruskal–Wallis test was used to compare the means among groups. Statistical significance was accepted at $P < 0.05$. If significant differences of mean values were detected, Tukey–Kramer or Scheffe multiple comparison analysis was used as a post hoc test.

Contact microradiogram and histology

The specimens were fixed in 70% ethanol, stained with Villanueva bone stain, dehydrated in graded ethanol, and embedded in methyl methacrylate. They were sectioned coronally using a low-speed saw machine (Isomet 5000; Buehler, Lake Bluff, IL, USA) with a diamond-wafering blade. The sectioned wafers were mounted on plastic slides and were ground and polished until they were 200–300 μm thick. Contact microradiography of undecalcified sections was carried out with a microradiography unit (Softex CMR Unit; Softex, Tokyo, Japan) for 60 s exposures, at 20 kV and 5 mA. After radiographs were taken, the polished wafers were ground and polished to 20–30 μm thickness and observed with a photomicroscope (Leica DFC300 FX, Leica Microsystems Japan, Tokyo, Japan).

Results

Macroscopic analysis

In the OCP/Col/Mesh group, the operated site was apparently augmented and bone-like hard tissue was palpated at the treated site; exposure of titanium mesh on the treated alveolar ridge was confirmed in two of three animals. In these cases, the alveolar ridge between the first and fourth premolars became thinner and frayed 1 month after operation. Although the area of exposed mesh was slightly increased with time, infectious symptoms such as swelling and pus discharge were hardly seen, and no sequestration was observed. In OCP/Col and untreated groups, the operated site was arc-shaped, and the atrophied alveolus was covered by healthy oral mucosa after 6 months of operation. No inflammatory and infectious symptoms were observed in either experimental group.

Chronological radiographic examination

Immediately after operation, the radiopaque bottom of the defect was similarly positioned in every group, and radiopacity in the OCP/Col implanted area was not clear without mesh-like radiopacity that corresponded to titanium mesh (Fig. 3). In the OCP/Col/Mesh group, a foggy radiopaque figure was observed in the implanted area at 2 months after operation, but it was distant from the top of the titanium mesh. At 6 months, the treated area was augmented with radiopacity that was similar to original bone. In the OCP/Col group, the radiopaque bottom of the defect was increased about 3–4 mm 2 months after operation, and a foggy radiopaque figure was observed at the OCP/Col implanted area. Subsequently, it increased and came to resemble original bone, whereas the bottom of the defect was stationary. In the untreated group, the radiopaque bottom of the defect was increased about 2–3 mm, immediately to 2 months after the operation; thereafter, no significant change was observed.

Morphometric analysis by micro-CT

In every group, the BMD of the operated region was similar to that of original bone,

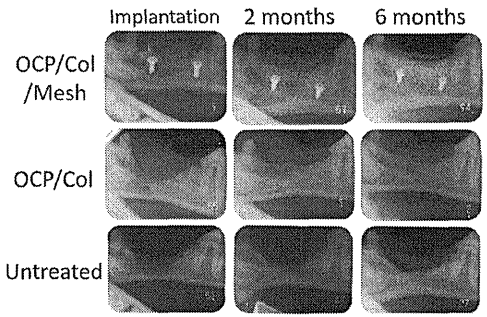

Fig. 3. Chronological radiographic examination of the treated defects. Immediately after operation, the radiopaque bottom of the defect is similarly positioned in every group. In the OCP/Col/Mesh group, a foggy radiopaque figure is observed in the implanted area at 2 months, but it is distant from the top of the titanium mesh. At 6 months, the treated area is augmented with radiopacity that is similar to original bone. In the OCP/Col group, the defect bottom is increased and a foggy radiopaque figure is observed in the OCP/Col implanted area at 2 months. At 6 months, it is increased and resembles original bone. In the untreated group, the radiopaque bottom of the defect is increased about 2–3 mm 2 months after surgery, thereafter no significant change is observed.

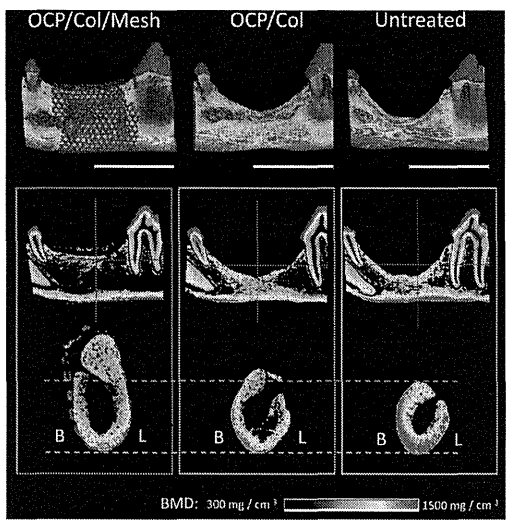

Fig. 4. BMD imaging of the defect in each experiment group. The vertical alveolar height of the operated region is apparently augmented in the OCP/Col/Mesh group more than in the OCP/Col and untreated groups. The operated mandible consists of outer cortical and inner cancellous structure as well as original bone. The newly formed bone in the OCP/Col/Mesh group seems to be regenerated along the covering of titanium mesh. The horizontal mandibular width of OCP/Col/Mesh- and OCP/Col-treated sites seems to be wider than that of the untreated group. B, buccal side; L, lingual side. Bars = 20 mm.

and the border between the original and newly formed bone in the operated region was hardly recognized. The operated mandible consisted of outer cortical and inner cancellous structures as well as original bone. The vertical alveolar height of the operated region was apparently augmented in the OCP/Col/Mesh group more than in the OCP/Col and untreated groups (Fig. 4). The augmented alveolus in the OCP/Col/Mesh group exhibited similar BMD to surrounding original bone. The newly formed bone in the OCP/Col/Mesh group seemed to regenerate along the covering of titanium mesh. The horizontal mandibular width of OCP/Col/Mesh- and OCP/Col-treated sites seemed to be wider than that of the untreated group. The bone volumes in the OCP/Col/Mesh, OCP/Col, and untreated groups were $1.22 \pm 0.132\ cm^3$, $0.821 \pm 0.0180\ cm^3$, and $0.643 \pm 0.0428\ cm^3$, respectively (Fig. 5a). As each group showed a normal distribution and all compared groups showed equal distributions, ANOVA was applied to compare mean values among the groups. A significant difference in mean value among these groups was shown (ANOVA, $F = 13.1$; df = 8; $P = 0.00645$) and Tukey–Kramer multiple comparison analysis as a post hoc test indicated significant differences between OCP/Col/Mesh and OCP/Col groups ($F = 3.45$; df = 6; $P = 0.0386$) and between OCP/Col/Mesh and untreated groups ($F = 5.00$; df = 6; $P = 0.00867$). The mandibular heights in OCP/Col/Mesh, OCP/Col, and untreated groups were 13.7 ± 1.19 mm, 11.0 ± 0.245 mm, and 9.66 ± 0.120 mm, respectively (Fig. 5b). As each group showed a normal distribution and compared groups showed unequal distributions, the Kruskal–Wallis test was applied to compare mean values among the groups. A significant difference in mean value among these groups was shown (Kruskal–Wallis, df = 2; $P = 0.0273$) and Scheffe multiple comparison analysis as a post hoc test indicated significant differences between OCP/Col/Mesh and untreated groups ($F = 8.14$; $P = 0.0195$). The mandibular widths in OCP/Col/Mesh, OCP/Col, and untreated groups were 7.21 ± 0.334 mm, 6.99 ± 0.706 mm, and 6.81 ± 0.407 mm, respectively (Fig. 5c). As each group showed a normal distribution and all compared groups showed equal distributions, ANOVA was applied to compare mean values among the groups. No significant difference in mean value among these groups was shown (ANOVA, $F = 0.228$; df = 8; $P = 0.803$).

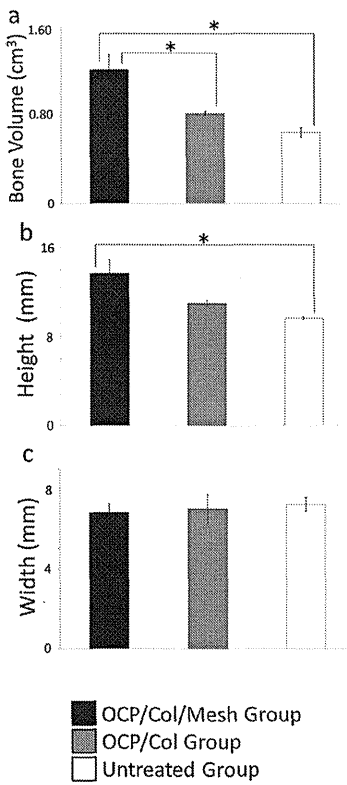

Fig. 5. Bone volume in the defect, mandibular height, and mandibular width of each experiment group. (a) The bone volumes in OCP/Col/Mesh, OCP/Col, and untreated groups were $1.22 \pm 0.132\ cm^3$, $0.821 \pm 0.0180\ cm^3$, and $0.643 \pm 0.0428\ cm^3$, respectively. A significant difference ($P < 0.05$) is seen between OCP/Col/Mesh and OCP/Col groups, and between OCP/Col/Mesh and untreated groups. (b) The mandibular heights in OCP/Col/Mesh, OCP/Col, and untreated groups are 13.7 ± 1.19 mm, 11.0 ± 0.245 mm, and 9.66 ± 0.120 mm, respectively. A significant difference ($P < 0.05$) is seen between OCP/Col/Mesh and untreated groups. (c) The mandibular widths in OCP/Col/Mesh, OCP/Col, and untreated groups are 7.21 ± 0.334 mm, 6.99 ± 0.706 mm, and 6.81 ± 0.407 mm, respectively. No significant difference in mean value among these groups is shown. Each group includes three samples. *$P < 0.05$.

Contact microradiographic and histology

In the OCP/Col/Mesh-treated alveolus, a radiopaque figure was observed along the inside of the area that was surrounded by titanium mesh (Fig. 6). The augmented radiopaque figure was clearly larger than in OCP/Col and untreated groups (Fig. 7). The proportion of radiolucent area in the augmented alveolus was greater than that in the original bone that was situated in the area of inferior mandibular border. Histologically, the augmented radiopaque area was almost completely occupied by matured bone tissue, and the remnant of implanted OCP/Col was hardly recognized. In the OCP/Col-treated alveolus, a small amount of vertically augmented radiopaque figure was observed at the OCP/Col implanted area. The proportion of radiolucent area in the alveolar crest was greater than that in the original bone. The augmented alveolus was almost completely occupied by matured bone tissue, and the small remnant of implanted OCP/Col was surrounded by regenerated bone tissue. In the untreated group, the created concave defect was transitionally repaired with surrounding soft tissues, and the repaired alveolar crest that was distinguished as bone tissue had a greater proportion of radiolucent area than that of the original bone.

Discussion

Macroscopically, the untreated and OCP/Col groups demonstrated atrophied alveolus at the operated site with healthy oral mucosa. This suggests that the implantation of OCP/Col *per se* in this mandibular defect was not involved in augmentation of alveolar height. The alveolus in the OCP/Col/Mesh group was augmented vertically more than in the OCP/Col and untreated groups because mechanical stress on the implanted OCP/Col was alleviated by covering the implant with titanium mesh. The dehiscence of alveolar mucosa in the OCP/Col/Mesh group was observed as previously reported.[19] This would be caused by blood flow decrease associated with stress on the alveolar ridge despite repose on tension-free closure and a soft food diet. It might also be caused by insufficient oral hygiene. Even if a high complication rate of exposure of the titanium mesh and dehiscence occurred in this experiment, these complications seemed to have little adverse effect on bone regeneration in these cases in the OCP/Col/Mesh group. Although it was reported that the exposure of titanium mesh with non-resorbable porous HA enhanced no new bone formation,[19] it was recently reported that the exposure of titanium mesh during healing did not necessarily compromise the final treatment outcome, because titanium mesh provides superior space maintenance and the pores within the titanium mesh are thought to play a critical role in maintaining blood supply to a grafted defect.[22] It should be clarified whether this phenomenon is specific for implantation of OCP/Col.

Chronological radiography in the treated defects immediately after operation showed the radiopaque bottom of the

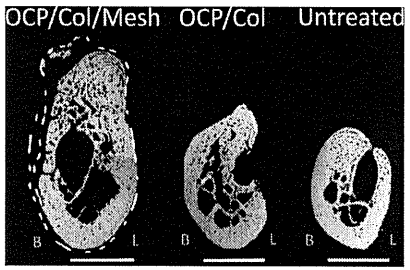

Fig. 6. Contact microradiographic examination. In the OCP/Col/Mesh-treated alveolus, the radiopaque figure is observed along the inside of the area that is surrounded by titanium mesh. The augmented radiopaque figure in the OCP/Col/Mesh group is clearly larger than those in the OCP/Col and untreated groups. B, buccal side; L, lingual side. Bars = 5 mm.

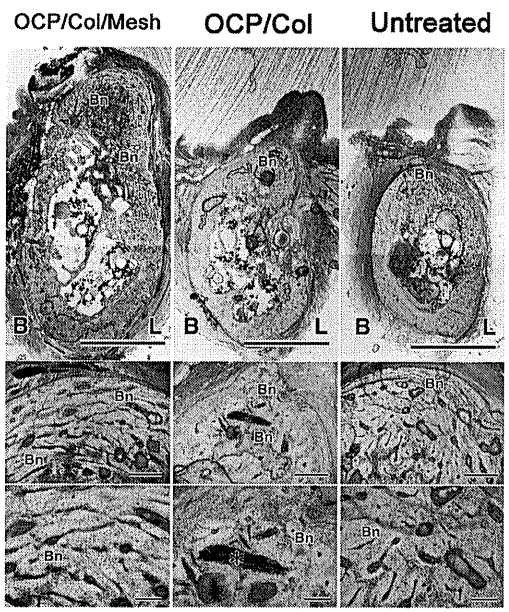

Fig. 7. Histological examination. The augmented alveolus in the OCP/Col/Mesh group is occupied by a large volume of matured bone (B), and the remnant of implanted OCP/Col is hardly recognized. The alveolus treated with OCP/Col is occupied by a small volume of matured bone (B), and a small amount of the remnant of implanted OCP/Col (*) is surrounded by regenerated bone tissue. In the untreated group, the concave defect created was transitionally repaired with surrounding soft tissues. Villanueva bone stain, *, implanted OCP; Bn, newly formed bone; B, buccal side, L, lingual side. Bars = 5 mm (upper row), 500 μm (middle row), 200 μm (lower row).

defect, which was similarly positioned in every group. Radiopacity in the OCP/Col implanted area was not clear. Although the radiopacity of the operated site showed no significant change in the untreated group during the observation periods, the OCP/Col-treated area in the OCP/Col and OCP/Col/Mesh groups indicated a foggy radiopacity at 2 months and came to resemble original bone at 6 months. This was due to apatitic conversion from OCP and/or bone regeneration by OCP/Col.[10] The increase of radiopacity on OCP/Col/Mesh was initiated from the bone defect or around the implanted OCP/Col. No active bone regeneration from the side of titanium mesh was observed. Therefore, titanium mesh would not be primarily involved with bone regeneration in the OCP/Col/Mesh group, although it was reported that titanium mesh as a space holder contributed to the osseous regeneration of the defect.[23]

In morphometric analysis by micro-CT, the bone volume in the OCP/Col/Mesh group was significantly higher than that in the OCP/Col and untreated groups. The mandibular height in the OCP/Col/Mesh group was significantly greater than that in the untreated group, whereas no significant difference in mandibular width was detected among the groups. These results suggest that vertical bone regeneration by OCP/Col was efficient and successful, if the mechanical stress to the implanted OCP/Col was alleviated by titanium mesh. Furthermore, it would be comparable to alveolar ridge augmentation in dogs with poly(D, L-lactic-co-glycolic acid) copolymer/gelatin sponge with recombinant human bone morphogenetic protein-2 (rhBMP-2).[24]

In every group, the newly formed bone in the operated region showed similar BMD as original bone, and the border between the original and newly formed bone in the operated region was hardly recognized. The augmented alveolus in the OCP/Col/Mesh group indicated similar BMD to surrounding original cortical bone, and the operated mandible consisted of outer cortical and inner cancellous structures as well as original bone. The newly formed bone in the OCP/Col/Mesh group seemed to be regenerated along the covering of titanium mesh. This suggests that most of the implanted OCP/Col would be replaced by cortical bone and the remaining part would be changed to cancellous bone through the course of physiological bone remodelling. Although BMD is considered to be correlated with bone strength,[25] it was reported that bone fracture risk was different according to age, gender, and ethnic group,[26] even with the same BMD value. Therefore it would be difficult to evaluate the mechanical characteristics of bone by using BMD value alone. Various evaluation methods might be used to establish bone strength and other bone qualitative factors.

The OCP/Col/Mesh-treated alveolus was clearly augmented by matured bone tissue along the inside of the titanium mesh, whereas the OCP/Col and untreated groups demonstrated unremarkable alveolar augmentation. This suggests that covering OCP/Col with titanium mesh clearly contributes to bone augmentation in this model, and alleviation of mechanical stress by titanium mesh would contribute to this process. In contact microradiograms, the proportion of radiolucent area in the regenerated alveolus was shown to be greater than that in the original bone in every group. This suggests that the observation period of 6 months would be midway through the healing process in this experimental model. As bone regeneration on the critical-sized calvarial defect in the canine model reached a plateau at 6 months after implantation of OCP/Col,[14] the specimen in this study was collected at that time. A longer observation period should be used to determine the fate of the regenerated bone in the OCP/Col/Mesh group.

In OCP/Col/Mesh and OCP/Col groups, the implanted OCP/Col almost disappeared and the remnant was hardly recognized 6 months after implantation. Recently, it was reported that OCP/Col was considerably resorbed in canine maxillary bone defect after 3 or 4 months of implantation,[12,13] whereas it distinctively remained in canine calvarial bone defects 12 months after implantation.[14] This suggests that biodegradation of OCP/Col depends on the OCP/Col implanted site.

This study indicated that bone regeneration by implantation of OCP/Col was enhanced when mechanical stress to the implant was alleviated. As recent studies reported that bone regeneration by OCP/Col was influenced by dehydrothermal treatment in the fabrication of OCP/Col or the composition of OCP and collagen,[20,27] development of greater bone regenerative property of OCP/Col, is anticipated. As OCP/Col is easy to handle and could promptly enhance bone regeneration without cell transplantation and exogenous osteogenic cytokines, clinical application of OCP/Col as a cost-effective bone regenerative material would avoid the harvesting of autogenous bone for grafting and provide a low-burden treatment for patients.

Funding

Although this study was supported in part by grants-in-aid (21592568, 20300165) from the Ministry of Education, Science, Sports and Culture of Japan and The HIROMI Medical Research Foundation, these study sponsors had no involvement in the study design; in the collection, analysis, and interpretation of data; in the writing of the manuscript; and in the decision to submit the manuscript for publication. In addition, the Animal Research Committee of Tohoku University approved all procedures in this study.

Competing interests

The authors (Kamakura and Suzuki) applied for a patent for OCP/Col in Japan.

Ethical approval

The Animal Research Committee of Tohoku University approved all procedures in this study.

Acknowledgments. The authors wish to thank Dr. Yuji Tanuma, Dr. Takuto Handa, Dr. Hiroshi Edamatsu, Dr. Naofumi Kanda, Dr. Kazuhito Kobayashi, and the Division of Oral Surgery, Department of Oral Medicine and Surgery, and Tohoku University Graduate School of Dentistry for their excellent assistance in this study.

References

1. Petite H, Viateau V, Bensaid W, Meunier A, de Pollak C, Bourguignon M, et al. Tissue-engineered bone regeneration. *Nat Biotechnol* 2000;**18**:959–63.
2. Miller LL, Kauffmann D, John DS, Wang DL, Grant JH, Waite PD. Retrospective review of 99 patients with secondary alveolar cleft repair. *J Oral Maxillofac Surg* 2010;**68**:1283–9.
3. Esposito M, Grusovin MG, Polyzos IP, Felice P, Worthington HV. Interventions for replacing missing teeth: dental implants in fresh extraction sockets (immediate, immediate-delayed and delayed implants). *Cochrane Database Syst Rev* 2010.
4. LeGeros RZ. Properties of osteoconductive biomaterials: calcium phosphates. *Clin Orthop Relat Res* 2002;**395**:81–98.
5. Ogose A, Kondo N, Umezu H, Hotta T, Kawashima H, Tokunaga K, et al. Histological assessment in grafts of highly purified beta-tricalcium phosphate (OSferion (R)) in human bones. *Biomaterials* 2006;**27**:1542–9.
6. Brown W, Smith J, Lehr J, Frazier A. Crystallographic and chemical relations between octacalcium phosphate and hydroxyapatite. *Nature* 1962;**196**:1050–5.
7. Suzuki O, Nakamura M, Miyasaka Y, Kagayama M, Sakurai M. Bone formation on synthetic precursors of hydroxyapatite. *Tohoku J Exp Med* 1991;**164**:37–50.
8. Suzuki O, Kamakura S, Katagiri T, Nakamura M, Zhao BH, Honda Y, et al. Bone formation enhanced by implanted octacalcium phosphate involving conversion into Ca-deficient hydroxyapatite. *Biomaterials* 2006;**27**:2671–81.
9. Kamakura S, Sasano Y, Shimizu T, Hatori K, Suzuki O, Kagayama M, et al. Implanted octacalcium phosphate is more resorbable than beta-tricalcium phosphate and hydroxyapatite. *J Biomed Mater Res* 2002;**59**:29–34.
10. Kamakura S, Sasaki K, Honda Y, Anada T, Suzuki O. Octacalcium phosphate combined with collagen orthotopically enhances bone regeneration. *J Biomed Mater Res B Appl Biomater* 2006;**79B**:210–7.
11. Kamakura S, Sasaki K, Homma T, Honda Y, Anada T, Echigo S, et al. The primacy of octacalcium phosphate collagen composites in bone regeneration. *J Biomed Mater Res A* 2007;**83A**:725–33.
12. Iibuchi S, Matsui K, Kawai T, Sasaki K, Suzuki O, Kamakura S, et al. Octacalcium phosphate (OCP) collagen composites enhance bone healing in a dog tooth extraction socket model. *Int J Oral Maxillofac Surg* 2010;**39**:161–8.
13. Matsui K, Matsui A, Handa T, Kawai T, Suzuki O, Kamakura S, et al. Bone regeneration by octacalcium phosphate collagen composites in a dog alveolar cleft model. *Int J Oral Maxillofac Surg* 2010;**39**:1218–25.
14. Kawai T, Matsui K, Iibuchi S, Anada T, Honda Y, Sasaki K, et al. Reconstruction of critical-sized bone defect in dog skull by octacalcium phosphate combined with collagen. *Clin Implant Dent Relat Res* 2011;**13**:112–23.
15. Rose FR, Oreffo RO. Bone tissue engineering: hope vs hype. *Biochem Biophys Res Commun* 2002;**292**:1–7.
16. Robling AG, Castillo AB, Turner CH. Biomechanical and molecular regulation of bone remodeling. *Ann Rev Biomed Eng* 2006;**8**:455–98.
17. Suzuki Y, Kamakura S, Honda Y, Anada T, Hatori K, Sasaki K, et al. Appositional bone formation by OCP–collagen composite. *J Dent Res* 2009;**88**:1107–12.
18. Matsui A, Anada T, Masuda T, Honda Y, Miyatake N, Kawai T, et al. Mechanical stress-related calvaria bone augmentation by onlayed octacalcium phosphate-collagen implant. *Tissue Eng Part A* 2010;**16**:139–51.
19. Eisig SB, Ho V, Kraut R, Lalor P. Alveolar ridge augmentation using titanium micromesh: an experimental study in dogs. *J Oral Maxillofac Surg* 2003;**61**:347–53.
20. Kawai T, Anada T, Honda Y, Kamakura S, Matsui K, Matsui A, et al. Synthetic octacalcium phosphate augments bone regeneration correlated with its content in

collagen scaffold. *Tissue Eng Part A* 2009;**15**:23–32.
21. Cao H, Kuboyama N. A biodegradable porous composite scaffold of PGA/beta-TCP for bone tissue engineering. *Bone* 2010;**46**: 386–95.
22. Her S, Kang T, Fien M. Titanium mesh as an alternative to a membrane for ridge augmentation. *J Oral Maxillofac Surg* 2012;**70**: 803–10.
23. Weng D, Hurzeler MB, Quinones CR, Ohlms A, Caffesse RG. Contribution of the periosteum to bone formation in guided bone regeneration. A study in monkeys. *Clin Oral Implants Res* 2000;**11**:546–54.
24. Kawakatsu N, Oda S, Kinoshita A, Kikuchi S, Tsuchioka H, Akizuki T, et al. Effect of rhBMP-2 with PLGA/gelatin sponge type (PGS) carrier on alveolar ridge augmentation in dogs. *J Oral Rehabil* 2008;**35**: 647–55.
25. Bouxsein ML, Courtney AC, Hayes WC. Ultrasound and densitometry of the calcaneus correlate with the failure loads of cadaveric femurs. *Calcif Tissue Int* 1995;**56**: 99–103.
26. Broussard DL, Magnus JH. Risk assessment and screening for low bone mineral density in a multi-ethnic population of women and men: does one approach fit all. *Osteoporos Int* 2004;**15**:349–60.
27. Kamakura S, Sasaki K, Honda Y, Anada T, Matsui K, Echigo S, et al. Dehydrothermal treatment of collagen influences on bone regeneration by octacalcium phosphate (OCP) collagen composites. *J Tissue Eng Regen Med* 2007;**1**:450–6.

Address:
Shinji Kamakura
Bone Regenerative Engineering Laboratory
Graduate School of Biomedical Engineering
Tohoku University
2-1 Seiryo-Machi
Aoba-Ku
Sendai 980-8574
Japan
Tel: +81 22 717 8235; Fax: +81 22 717 8235
E-mail: kamakura@bme.tohoku.ac.jp

Contents lists available at SciVerse ScienceDirect

Clinical Neurophysiology

journal homepage: www.elsevier.com/locate/clinph

Auditory evoked magnetic fields in patients with absent brainstem responses due to auditory neuropathy with optic atrophy

Yusuke Takata [a,*], Tetsuaki Kawase [a,b,c], Nobukazu Nakasato [d,e], Akitake Kanno [f,g], Toshimitsu Kobayashi [a]

[a] Department of Otolaryngology-Head and Neck Surgery, Tohoku University Graduate School of Medicine, 1-1 Seiryo-machi, Aoba-ku, Sendai 980-8574, Japan
[b] Laboratory of Rehabilitative Auditory Science, Tohoku University Graduate School of Biomedical Engineering, Sendai 980-8574, Japan
[c] Department of Audiology, Tohoku University Graduate School of Medicine, Sendai 980-8574, Japan
[d] Department of Epileptology, Tohoku University Graduate School of Medicine, Sendai 980-8575, Japan
[e] Department of Electromagnetic Neurophysiology, Smart Ageing International Research Center, Institute of Development, Aging and Cancer, Tohoku University, 4-1 Seiryo-cho, Aoba-ku, Sendai 980-8575, Japan
[f] Department of Functional Brain Imaging, Institute of Development, Aging and Cancer, Tohoku University, 4-1 Seiryo-cho, Aoba-ku, Sendai 980-8575, Japan
[g] MEG Laboratory, Kohnan Hospital, 4-20-1 Nagamachi-minami, Taihaku-ku, Sendai 982-8523, Japan

ARTICLE INFO

Article history:
Accepted 23 October 2011
Available online 26 November 2011

Keywords:
Auditory neuropathy
Magnetoencephalography
Auditory evoked
field
N100m

HIGHLIGHTS

- Auditory evoked fields were measured in three patients with auditory neuropathy and optic atrophy showing absence of auditory brainstem responses.
- Bihemispherical AEF responses were clearly recorded in all patients for either left or right ear stimulus.
- Presence and abnormality of auditory cortical responses can be evaluated by AEFs in patients with auditory neuropathy even in the absence of ABRs.

ABSTRACT

Objective: To examine whether auditory evoked fields (AEFs) can be used to objectively evaluate hearing in patients with absent auditory brainstem responses (ABRs) due to auditory neuropathy.
Methods: Subjects were 3 patients with auditory neuropathy, 1 male aged 29 years and 2 females aged 18 and 27 years, with absence of click evoked ABRs for bilateral ear stimuli at a level of 105 dB nHL. All patients also had optic atrophy. AEFs were measured with a helmet-shaped magnetoencephalography system for 2.0 kHz tone bursts of 60 ms duration to the unilateral ear.
Results: Bihemispherical AEF responses were clearly recorded in all three patients for either left or right ear stimulus. Although the latencies of N100m were severely prolonged and amplitudes were considerably decreased compared to the normal range of N100m responses in our facilities, N100m latency of AEF was shorter in the contralateral hemisphere to the stimulated ear, as usually found in normal subjects, despite the abnormal delay in N100m latency in all conditions.
Conclusions: Presence and abnormality of auditory cortical responses can be evaluated by AEFs in patients with auditory neuropathy even under null responses in ABRs.
Significance: AEFs are useful to evaluate residual hearing in patients with auditory neuropathy.

1. Introduction

Auditory neuropathy is a type of sensorineural hearing loss which is characterized by absence or marked abnormalities of auditory brainstem responses (ABRs) beyond that expected for the degree of hearing loss, with preserved activity of the outer hair cells in the inner ear, including otoacoustic emissions (OAEs) and/or cochlear microphonics (CM) (Starr et al., 1996; Kaga et al., 1996). Psychophysically, word discrimination is impaired and disproportional to the pure-tone audiogram in these patients (Starr et al., 1996).

Auditory neuropathy includes many different etiologies causing absence of ABR with intact outer hair cell function (Doyle et al., 1998; Rance et al., 1999; Miyamoto et al., 1999; Bähr et al., 1999; Varga et al., 2003, 2006; Berg et al., 2005; Vlastarakos et al., 2008). The hearing loss caused by auditory neuropathy may be non-syndromic, in which the symptom is isolated, or syndromic, as a part of the symptoms associated with known hereditary neurological disorders, such as Charcot-Marie-Tooth disease, Friedrich's ataxia, mitochondrial disease, and autosomal dominant optic atrophy (ADOA), or secondary to general pathology such as hyperbilirubinemia, anoxia, and viral infection (Singh et al., 1989; Starr et al., 2000; Ceranić and Luxon, 2004; Amati-Bonneau et al., 2005; Brookes et al., 2008; Huang et al., 2009; Meyer et al., 2010; Mizutari et al., 2010; Cacace and Pinheiro, 2011).

* Corresponding author. Tel.: +81 22 717 7303; fax: +81 22 717 7307.
E-mail address: ent2003jp@yahoo.co.jp (Y. Takata).

1388-2457/$36.00 © 2011 International Federation of Clinical Neurophysiology. Published by Elsevier Ireland Ltd. All rights reserved.
doi:10.1016/j.clinph.2011.10.044

The exact pathophysiology of auditory neuropathy remains unknown, but one key pathology type is thought to be synaptic dysfunction between the inner hair cells in the inner ear and the primary auditory neurons (Trussell, 1999; Khimich et al., 2005; Sterling and Matthews, 2005). However, the characteristic findings of auditory neuropathy such as absent ABR as well as poor speech perceptibility may result from desynchronized auditory nerve activity (Berlin et al., 2001, 2003). Therefore, auditory neuropathy has been described as auditory dys-synchrony.

Neural synchrony is important in recording auditory evoked responses, but the effects of dys-synchrony may vary with the different evoked responses; i.e., auditory N100 and P200 cortical sensory potentials to tones could be often obtained with delayed latency, despite the absence of ABR (Satya-Murti et al., 1983; Kraus et al., 1993; Starr et al., 1996, 2003, 2004; Rance et al., 2002; Michalewski et al., 2005). Differences in the degradation of such cortical responses may indicate variations in the dys-synchrony of the auditory nerve activity, so detailed assessment of the cortical response in auditory neuropathy may be important. Cortical responses in patients with auditory neuropathy have been examined by conventional electroencephalography (EEG) (Satya-Murti et al., 1983; Kraus et al., 1993; Starr et al., 1996, 2003, 2004; Rance et al., 2002; Michalewski et al., 2005) using minimal electrodes (Fz, Cz, Pz, etc.), so the recordings were not intended to analyze the right and left cortical responses separately. However, the effects of peripheral events on the auditory cortex may be different between the right and left hemispheres (Wienbruch et al., 2006; Morita et al., 2007; Hiraumi et al., 2008), so separate analysis of the bilateral cortical responses, which is possible by multichannel recording using EEG and/or magnetoencephalography (MEG), may provide additional information about the auditory cortical responses in patients with auditory neuropathy.

In the present study, the auditory N100m responses were measured by multichannel MEG in three patients with auditory neuropathy and optic atrophy (neuropathy) (Hari et al., 1980; Pantev et al., 1986; Näätänen and Picton, 1987; Reite et al., 1994; Pantev et al., 1995; Nakasato et al., 1995, 1997; Kanno et al., 1996; Kanno et al., 2000), to investigate the detailed abnormal cortical responses associated with sensorineural hearing loss caused by retrocochlear lesion, which is characterized by dys-synchrony.

2. Materials and methods

2.1. Subjects

This study included 3 patients, 1 male aged 29 years (Case 1) and 2 females aged 18 years (Case 2) and 27 years (Case 3), with auditory neuropathy diagnosed in the Department of Otolaryngology-Head and Neck Surgery, Tohoku University Hospital (indicated ages at N100m measurement). The diagnosis of auditory neuropathy was based on the following findings: absence or marked abnormalities of ABRs beyond that expected for the degree of hearing loss; and preserved outer hair cell activity including OAEs and/or CM. Clinical courses and background data of the participants are summarized in Table 1 and Fig. 1. All three subjects also had optic atrophy. Optic atrophies or optic neuropathies form a group of disorders that are characterized by visual loss due to retinal ganglion cell death (Meyer et al., 2010). Optic atrophy is often associated with auditory neuropathy in several genetic disorders, such as ADOA, Leber's hereditary optic atrophy, and deafness–dystonia–optic neuropathy syndrome (Singh et al., 1989; Ceranić and Luxon, 2004; Amati-Bonneau et al.,

Table 1
Clinical courses of three subjects.

Case	Hearing disturbance			Visual disturbance			Vestibular symptoms	Other neurological symptoms	Social activity (present)	Genetic examination	Communication method (present)	Family history
	Diagnosis	Onset (first noticed)	First visit to our oto-laryngology	Diagnosis	Onset (first noticed)	First visit to our ophthalmology	Clinical course (see also Fig. 1)					
1	AN	Around 15 y.o.	15 y.o. (7 y.o for screening)	Optic atrophy	Around 5 y.o.	7 y.o.	Already considerably deteriorated at first visit	None (vestibular function test: not done)	None (no apparent abnormality indicated by pediatricians at 7 y.o.)	Office worker (using a computer for visual impaired)	Mitochondrial DNA (negative 3243 [A-C] 1555 [A-C] mutations)	Hearing aid + writing	Sister (Case 3) and father (hearing and visual disturbance)
2	AN	Around 10 y.o.	11 y.o.	Fluctuant	Optic atrophy	Around 6 y.o.	11 y.o.	Already considerably deteriorated at first visit	None (vestibular function test: not done)	None without Babinski (+) (examined in pediatric neurology including NCV*)	Clerical staff	Not done	Writing (hearing aid is not effective)	None
3	AN	Around 10 y.o.	18 y.o.	Relatively stable after first visit	Optic atrophy	Around 6 y.o.	11 y.o.	Already considerably deteriorated at first visit	None (vestibular function test: not done)	None	Massage therapist	Not done	Hearing aid + writing	Brother (Case 1) and father (hearing and visual disturbance)

AN: auditory neuropathy, y.o.: years old.
* NCV (nerve conduction velocity): motor nerve conduction velocity for median nerve and sensory conduction velocity for tibial nerve were examined in Case 2.

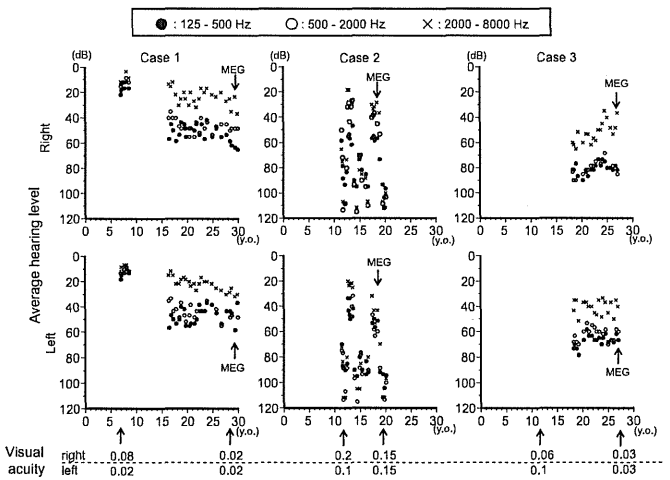

Fig. 1. Clinical course of hearing and visual acuity. Average hearing level for low (average threshold for 125, 250, and 500 Hz), mid (average threshold for 500, 1000, and 2000 Hz), high (average threshold for 2000, 4000, and 8000 Hz) frequency regions are plotted as a function of age of the patients. Visual acuities at first visit and at latest visit are also indicated at the bottom.

2005; Brookes et al., 2008; Huang et al., 2009; Mizutari et al., 2010; Cacace and Pinheiro, 2011), so genetic testing is usually recommended for abnormalities such as OPA1 gene and/or 11,778 mitochondrial DNA point mutation, which are known to cause the ADOA and Leber's hereditary optic atrophy, respectively (Singh et al., 1989; Amati-Bonneau et al., 2005; Huang et al., 2009; Mizutari et al., 2010; Cacace and Pinheiro, 2011). Unfortunately, our patients refused such genetic testing, so no genetic information was obtained except for the absence of mutation of mitochondrial DNA at 3243 and 1555 in Case 1, which was identified 11 years previously. At that time, available genetic testing was very limited in our laboratory and this genetic test was performed to screen for hearing loss due to genetic disorder. Cases 1 and 3 are siblings, with relatively stable hearing levels since the first visit to our department for hearing disturbance. In contrast, Case 2 had very fluctuant hearing. The exact reason for this hearing instability remains unknown. However, we suspected the possible presence of functional hearing loss, based on the discrepancy between the change in hearing level and subjective audibility. The present study was approved by the ethical committee of the Tohoku University Graduate School of Medicine. All parts of the present study were performed in accordance with the guidelines of the Declaration of Helsinki.

2.2. Otological examinations

The patients were interviewed to establish any history of hearing loss, followed by ear, nose, and throat examination, then pure-tone audiometry followed by measurements of distortion product OAEs, ABRs, and magnetic resonance (MR) imaging.

2.3. Measurement of auditory evoked fields (AEFs)

AEFs were recorded with a 160-channel whole-head type axial gradiometer system (MEGvision PQ1160c; Yokogawa Electric, Musashino, Tokyo, Japan) in a magnetically shielded room (Daido Steel Co., Ltd., Nagoya, Aichi, Japan) in the awake condition. The sensors of this system are configured as first-order axial gradiometers with a baseline of 50 mm; each coil of the gradiometers measures 15.5 mm in diameter. The sensors are arranged in a uniform array on a helmet-shaped surface at the bottom of the dewar and the mean distance between the centers of two adjacent coils is 25 mm. The stimulus to elicit the N100m response was a tone burst of 60 ms duration (rise and fall times of 10 ms, plateau time of 40 ms) at a frequency of 2 kHz and presented monaurally. The sound pressure level of the tone bursts was presented at 80 dB SPL at first. However, if no apparent N100m could be obtained at 80 dB SPL, then the sound level was increased in 10 dB steps up to 110 dB SPL until the N100m response was obtained. The minimum sound level to obtain the apparent N100m was defined as the detection threshold of N100m. Continuous masking noise (white noise) was applied to the contralateral ear. The level of masking noise was set at 30 dB below the stimulus level. Both ears were measured in all three patients. The signal and masking noises were presented to the subject through canal earphones (ER-3A; Etymotic Research, Elk Grove Village, IL). The mean interstimulus interval was 3.33 s (0.3 Hz) with 50% interstimulus variance. The AEFs were recorded only in the awake state as confirmed by real time monitoring of the occipital alpha rhythm by MEG. The MEG signal was band-pass filtered between 0.03 and 400 Hz, and sampled at 1250 Hz. The data from 100 ms before to 500 ms after the stimulus onset were averaged 50 times. The averaged data were digitally band-pass filtered from 2.0 to 20.0 Hz in the following off-line analysis.

The present study focused on the N100m response in adult patients with auditory neuropathy. The N100m response is the magnetic counterpart of the N1/N100 in EEG (Pantev et al., 1995). Peak latencies of the N100m responses were derived from the maximal root-mean-square value calculated on the basis of all

channels of all sessions. The location of each source was estimated at the N100m peak latency, using an equivalent current dipole (ECD) model with the best fit sphere for each subject's head. The source location was superimposed on the three-dimensional MR image of the individual subject using a MEG–MR image coordination integration system. The N100m response was identified as the first peak with latency longer than 80 ms based on the two criteria, the isofield map had the downward current orientation, and the estimated location of the current source by the ECD model was superimposed onto the auditory cortex on the three-dimensional MR image of the individual subject, which are known characteristics of the N100m in MEG (Hari et al., 1980; Pantev et al., 1986; Näätänen and Picton, 1987; Reite et al., 1994; Pantev et al., 1995; Nakasato et al., 1995, 1997; Kanno et al., 1996, 2000).

The amplitudes of the N100m responses in our subjects were often much smaller than those in normal subjects, sometimes nearly as low as noise level, and the N100m response was sometimes hard to identify based only on the conventional time-axis wave form, which is the usual way to identify N1/N100 in conventional EEG. However, even in such cases, the N100m could be clearly identified in MEG measurements by searching for the response peak fulfilling the above-mentioned N100m criteria, which is one of the advantages in using MEG to analyze the N100 response instead of the conventional EEG method.

Since the number of the patients examined in the present study was too small for statistical analysis, the abnormality of the N100m responses (at the maximum amplitude channel of each hemisphere) was determined based on the normal range of N100m responses at the maximum amplitude channel of each hemisphere in our facilities (Kohnan Hospital), which was defined for practical reasons as the mean ± 2 standard deviations of 37 normal subjects (31 males and 6 females, aged from 21 to 59 years [mean 31.0 years]).

3. Results

The findings of AEFs, audiograms, ABRs, and OAEs are shown in Figs. 2 and 3, and Table 2. The sound levels shown in Table 2 indicate the minimum sound level to obtain the apparent N100 m, that is the detection threshold. Measurement of auditory evoked magnetic fields to both ear stimuli in the contralateral hemispheres at the detection threshold levels are represented in Fig. 3, which shows the N100 m responses, isofield patterns, and the estimated ECDs of the contralateral ear stimuli. The degree of hearing loss in the audiogram varied with the patient, but the ABRs were absent and the distortion product OAEs were normal in all patients. Word discrimination scores were lower than expected from the degrees of hearing loss.

N100m responses in both the ipsilateral and contralateral hemispheres to the stimuli of either ear were compatible with the auditory response because of the ECD location in all patients (Table 2). The source of the N100m was localized in the primary auditory cortex along the superior temporal plane in each hemisphere for either ear stimuli. N100m responses were recorded in all cases, but the latencies were severely prolonged and the amplitudes were considerably decreased compared to the normal range of N100m responses in our facilities. However, despite the abnormal responses, the latencies of N100m were shorter for the contralateral than the ipsilateral stimuli as usually observed in normal subjects (Elberling et al., 1981, 1982; Reite et al., 1981; Pantev et al., 1986; Mäkelä et al., 1994; Nakasato et al., 1995). N100m responses observed in the contralateral hemispheres to the stimuli are shown as stacked waveforms in Fig. 3, in addition to the isofield patterns over the entire head and the estimated ECDs at the peak latency in the contralateral hemisphere, which are superimposed onto the individual horizontal and coronal MR images. Fig. 4 shows the relationships between average hearing level, speech intelligibility, and the detection threshold of N100m.

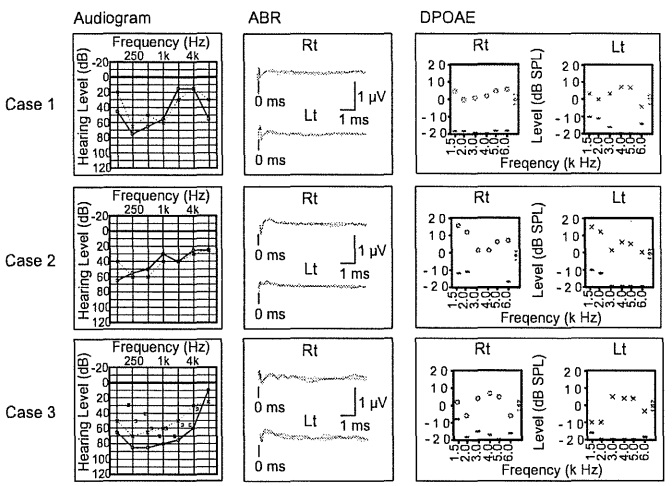

Fig. 2. Audiogram, ABR, and distortion product OAE (DPOAE) measured at the nearest point to the N100m measurements. ABRs to 105 dB nHL clicks were measured three times. All ears had absent ABRs, but hearing in audiograms was relatively preserved and DPOAEs were normal in each patient.

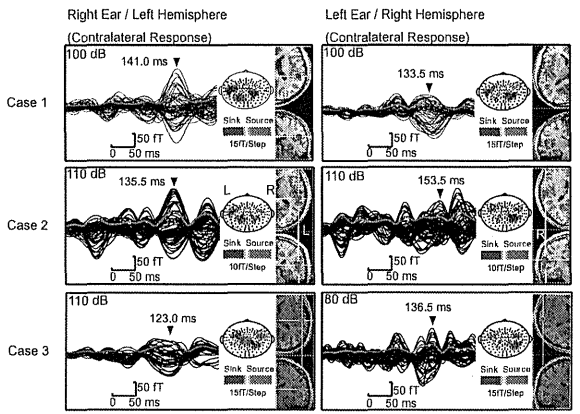

Fig. 3. Measurement of auditory evoked magnetic fields to both ear stimuli in the contralateral hemispheres. The N100m responses, isofield patterns, and estimated ECDs are indicated. Stacked waveforms show the N100m responses. The peak latencies of N100m (arrowhead) are derived from the maximum root-mean-square value (red line). Isofield patterns over the entire head, viewed from above, are shown above the waveforms: red contours (magnetic flux-out) and blue contours (magnetic flux-in) are shown with contour step of 15 fT in Case 1, 10 fT in Case 2, and 15 fT in Case 3 at the peak latency. Estimated ECDs superimposed onto the subject's MR images (panel right side, upper: horizontal and lower: coronal views). Note that the ECDs are located in the primary auditory cortices.

Table 2
Clinical characteristics of the patients with auditory neuropathy.

Case	Age (y) */Sex	Ear side	PTA (dB)	Word%	DPOAE	ABR	Normal range			
							N100m latency		N100m amplitude	
							Right hemisphere	Left hemisphere	Right hemisphere	Left hemisphere
							Right ear stimulation			
							77.8–116.6 ms	68.5–108.5 ms	350–461.6 fT	319.6–431.6 fT
							Left ear stimulation			
							66.4–101.2 ms	83.7–120.1 ms	427.6–541.2 fT	265.5–364.7 fT
1	29/M	Right	45	25% 90 dB	Normal	Absent	100 dB 148.5 ms	100 dB 141.0 ms	100 dB 85.2 fT	100 dB 145.3 fT
		Left	46.7	20% 80 dB	Normal	Absent	100 dB 133.5 ms	100 dB 151.0 ms	100 dB 95.1 fT	100 dB 133.8 fT
2	18/F	Right	40	30% 100 dB	Normal	Absent	110 dB 150.0 ms	110 dB 135.5 ms	110 dB 90.0 fT	110 dB 157.2 fT
		Left	46.7	20% 50 dB	Normal	Absent	110 dB 153.5 ms	110 dB 169.5 ms	110 dB 101.0 fT	110 dB 80.5 fT
3	27/F	Right	80	25% 100 dB	Normal	Abnormal**	110 dB 129.5 ms	110 dB 123.0 ms	110 dB 91.3 fT	110 dB 78.2 fT
		Left	58.3	40% 70 dB	Normal	Absent	80 dB 136.5 ms	80 dB 141.0 ms	80 dB 99.0 fT	80 dB 54.0 fT

PTA = pure tone average (threshold average for frequencies of 0.5, 1.0, and 2.0 kHz).
Word% = word discrimination score (word% correct).
DPOAE = distortion product otoacoustic emission.
ABR = auditory brainstem response.
N100m amplitude: N100m response at the maximum amplitude channel of each hemisphere. Normal range of N100m latency and N100m amplitude (for 2000 Hz tone bursts at a level of 80 dB SPL) in our facility are indicated in shaded area (average ± 2 standard deviation) (Kanno et al., 1996).
* Age: age at MEG measurement.
** Suspected cochlear microphonics were indicated.

4. Discussion

In the present study, N100m peaks in response to 2.0 kHz tone bursts were detected in the bilateral hemispheres of all three patients, despite the absence of click evoked ABRs (at 105 dB nHL). The latencies were severely prolonged and the amplitudes were considerably decreased compared to the normal range of N100m responses in our facilities, but shorter latencies were observed in the hemisphere contralateral to the stimulated ear compared with those in the hemisphere ipsilateral to the stimulated ear, as usually found in normal subjects. EEG has already suggested the presence of cortical responses in auditory neuropathy subjects with absent ABR (Starr et al., 1996; Michalewski et al., 2005). However, cortical responses were not analyzed for the separate hemispheres in these EEG studies. Such separate analysis of the bilateral cortical responses is worthwhile considering that the effects of peripheral events on the auditory cortex may be different between the right and left hemispheres (Wienbruch et al., 2006; Morita et al., 2007; Hiraumi et al., 2008). The assessment of cortical response by MEG would also be essential for further observing the effects of

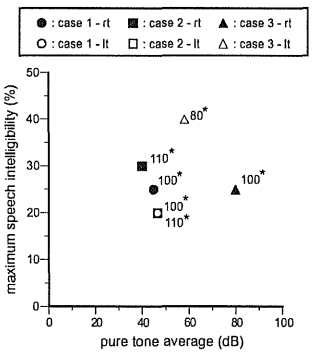

Fig. 4. Relationships between average hearing level, speech intelligibility, and the detection threshold of N100m. Maximum speech intelligibility is plotted as a function of pure tone average (500–2000 Hz) for each ear, and detection threshold level for each ear is shown for each symbol (marked with asterisks). N100m in response to 2 kHz tone-burst at a level of 80 dB SPL was only observed in the left ear of Case 3, in whom the best speech discrimination (40%) was obtained among the 6 ears of the 3 patients, although the hearing threshold at 2 kHz was worse than those of Cases 1 and 2, in whom stimuli at 100 dB or higher were needed to measure robust N100m response.

auditory dys-synchrony on other types of cortical response with hemispheric asymmetry, such as the auditory steady state response in response to amplitude modulation tone and cortical responses to speech stimuli.

MEG has evolved from a single-channel portable system to modern whole head systems providing an advanced and powerful method for direct and noninvasive brain function research (Bagic et al., 2009). The critical locations of AEFs can also be identified accurately with MEG (Romani et al., 1982; Alberstone et al., 2000; Nakasato and Yoshimoto, 2000; Godey et al., 2001). MEG is less prone to distortion than EEG, because the skull and other extracerebral tissues substantially affect electrical current fields in EEG, but are practically transparent to magnetic fields (Soeta and Nakagawa, 2009). Dipolar source analysis based on MEG can also effectively isolate the lateralized nature of auditory evoked potentials (Huang et al., 2003), which is an important advantage of MEG measurement in patients with pathology, since any delayed latency responses with deteriorated signal to noise ratio can be correlated with the auditory evoked N100m responses originating from the primary auditory cortices, based on the ECD locations with the best fit sphere for each subject's head (Hari et al., 1980; Pantev et al., 1986; Näätänen and Picton, 1987; Reite et al., 1994; Pantev et al., 1995; Nakasato et al., 1995; Kanno et al., 1996; Nakasato et al., 1997; Kanno et al., 2000).

The presence or absence of cortical responses and speech intelligibility may be related, as indicated in a previous study of young children with auditory neuropathy (Rance et al., 2002). The present study included too few cases to analyze the relationship between speech intelligibility and N100m response, but did appear to indicate similar trends. As shown in Table 2 and Fig. 4, the N100m in response to 2 kHz tone-burst at a level of 80 dB SPL was only observed in the left ear of Case 3, in whom the best speech discrimination (40%) was obtained among the 6 ears of the 3 patients, although the hearing threshold at 2 kHz was worse than those of Cases 1 and 2, in whom stimuli at 100 dB or higher were needed to measure robust N100m response. These results indicate that the measurement of cortical responses could be useful to assess the auditory pathophysiology in patients with auditory neuropathy. The relationship between the clinical characteristics and the parameters of the N100m response such as latency and amplitude also raises intriguing questions. These parameters were severely deteriorated in the present patients and would be expected to indicate some pathological conditions. However, these parameters are also affected by the hearing level and stimulation level, so further investigations using much more data are required to analyze these issues.

Auditory neuropathy includes many different etiologies causing absence of the ABR associated with intact outer hair cell function, such as synaptic dysfunction between the inner hair cells in the inner ear and the primary auditory neurons (Doyle et al., 1998; Rance et al., 1999; Miyamoto et al., 1999; Bähr et al., 1999; Trussell, 1999; Varga et al., 2003; Berg et al., 2005; Khimich et al., 2005; Sterling and Matthews, 2005; Varga et al., 2006; Vlastarakos et al., 2008). Therefore, analysis of the neurophysiological and psychophysical data based on the individual etiology would be preferable. Classification based on genetic disorders is a potentially useful way to categorize the etiology of auditory neuropathy. In our cases, the involvement of some specific genetic disorder is possible, since two of our patients were siblings, and all patients had similar clinical features including association with optic atrophy, age of onset of visual and hearing disturbances, and others. Unfortunately, we have no useful data on the genetic background relating to the etiology, so this aspect requires further study.

One mechanism which may explain the characteristic findings of auditory neuropathy is "desynchronized auditory nerve activity", which is caused by pathological dysfunction of the synapses between the inner hair cells and the auditory neurons or demyelinization of the auditory nerve (Starr et al., 1991; Berlin et al., 2001, 2003). The resultant de-synchronization of the spike timing between neurons deteriorates the wave formation of the ABR, which is the sum of the synchronized spike activities of the neurons evoked by sound stimuli. Investigation of the effects of de-synchronization on the ABR waveform with cats suggested that 1-ms jitter between the click stimuli and the averaging process can abolish the ABR waveforms (Starr et al., 1991). Therefore, dys-synchrony on the order of 1 ms could abolish the ABR wave even though the sound can be heard. On the other hand, the cortical auditory evoked response of N100m, which is also a synchronized response to tone, can be detected in patients with auditory neuropathy with absent ABR. The presence of the cortical auditory evoked response in patients with absent ABR may reflect different redundancies in temporal neural processing between the auditory cortex and brainstem or different susceptibility to "dys-synchrony" between the ABR and cortical response.

The different susceptibility of the ABR and the N100m may be partly explained by the different configurations of the response waves; i.e., comparison of the "duration" (duration between the onset and the endpoint of each wave) of the ABR and N100m response found that the duration of the ABR was much shorter (about 1/100) than that of the N100m response, based on data obtained in our facilities: average wave duration was 63.0 ± 11.3 ms (n = 20) for N100 m, 0.58 ± 0.1 ms (n = 20) for wave I of ABR, and 0.89 ± 0.2 ms (n = 20) for wave V. Therefore, the effects of "dys-synchrony" might be much larger on the ABR waveform than on the N100m. In fact, similar measurements concerning the effects of jitter between the onset of tone bursts and the averaging process on the N100m waveforms support this hypothesis; i.e., the amplitude of N100m waveform was little affected by jitter of 10–20 ms duration between the stimuli and averaging process, whereas jitter of longer duration was associated with reduced N100m amplitude, and jitter of 80 ms duration resulted in the N100m wave being almost completely abolished (unpublished data). Therefore, the

degree of abnormality observed in the N100m response may also reflect the dys-synchrony of the auditory fiber, so that more severe abnormality of the N100m indicates more severe pathophysiology of the auditory nerve. In this context, detailed measurements of the N100m responses including the response thresholds as well as response growth functions can be expected to provide more useful information concerning the pathophysiology of the patients with auditory neuropathy, although only the N100m responses to relatively high sound levels were examined in the present study.

Acknowledgements

We wish to thank the staff of Kohnan Hospital Ryogo Center for their continuous support of this work. This study was supported by a Grant from the Ministry of Education, Culture, Sports, Science and Technology – Japan (Grant-in-Aid for Exploratory Research 15659401).

References

Alberstone CD, Skirboll SL, Benzel EC, Sanders JA, Hart BL, Baldwin NG, et al. Magnetic source imaging and brain surgery: presurgical and intraoperative planning in 26 patients. J Neurosurg 2000;92:79–90.
Amati-Bonneau P, Guichet A, Olichon A, Chevrollier A, Viala F, Miot S, et al. OPA1 R445H mutation in optic atrophy associated with sensorineural deafness. Ann Neurol 2005;58:958–63.
Bagic A, Funke ME, Ebersole J. American Clinical MEG Society (ACMEGS) position statement: the value of magnetoencephalography (MEG)/magnetic source imaging (MSI) in noninvasive presurgical evaluation of patients with medically intractable localization-related epilepsy. J Clin Neurophysiol 2009;26:290–3.
Bähr M, Andres F, Timmerman V, Nelis ME, Van Broeckhoven C, Dichgans J. Central visual, acoustic, and motor pathway involvement in a Charcot-Marie-Tooth family with an Asn2055er mutation in the connexin 32 gene. J Neurol Neurosurg Psychiatry 1999;66:202–6.
Berg AL, Spitzer JB, Towers HM, Bartosiewicz C, Diamond BE. Newborn hearing screening in the NICU: profile of failed auditory brainstem response/passed otoacoustic emission. Pediatrics 2005;116:933–8.
Berlin CI, Hood LJ, Rose K. On renaming auditory neuropathy as auditory dys-synchrony. Audiol Today 2001;13:15–7.
Berlin CI, Hood LJ, Morlet T, Rose K, Brashears S. Auditory neuropathy/dys-synchrony: diagnosis and management. Ment Retard Dev Disabil Res Rev 2003;9:225–31.
Brookes JT, Kanis AB, Tan LY, Tranebjaerg L, Vore A, Smith RJ. Cochlear implantation in deafness–dystonia–optic neuronopathy (DDON) syndrome. Int J Pediatr Otorhinolaryngol 2008;72:121–6.
Cacace AT, Pinheiro JM. The mitochondrial connection in auditory neuropathy. Audiol Neurootol 2011;16:398–413.
Ceranić B, Luxon LM. Progressive auditory neuropathy in patients with Leber's hereditary optic neuropathy. J Neurol Neurosurg Psychiatry 2004;75:626–30.
Doyle KJ, Siniger Y, Starr A. Auditory neuropathy in childhood. Laryngoscope 1998;108:1374–7.
Elberling C, Bak C, Kofoed B, Lebech J, Saermark K. Auditory magnetic fields from the human cortex. Influence of stimulus intensity. Scand Audiol 1981;10:203–7.
Elberling C, Bak C, Kofoed B, Lebech J, Saermark K. Auditory magnetic fields from the human cerebral cortex: location and strength of an equivalent current dipole. Acta Neurol Scand 1982;65:553–69.
Godey B, Schwartz D, de Graaf JB, Chauvel P, Liegeois-Chauvel C. Neuromagnetic source localization of auditory evoked fields and intracerebral evoked potentials: a comparison of data in the same patients. Clin Neurophysiol 2001;112:1850–9.
Hari R, Attoniemi K, Jarvinen MJ, Katila T, Varpula T. Auditory evoked transient and sustained magnetic fields of the human brain: localization of neural generators. Exp Brain Res 1980;40:237–40.
Hiraumi H, Nagamine T, Morita T, Naito Y, Fukuyama H, Ito J. Effect of amplitude modulation of background noise on auditory-evoked magnetic fields. Brain Res 2008;1239:191–7.
Huang MX, Edgar JC, Thoma RJ, Hanlon FM, Moses SN, Lee RR, et al. Predicting EEG responses using MEG sources in superior temporal gyrus reveals source asynchrony in patients with schizophrenia. Clin Neurophysiol 2003;114:835–50.
Huang T, Santarelli R, Starr A. Mutation of OPA1 gene causes deafness by affecting function of auditory nerve terminals. Brain Res 2009;1300:97–104.
Kaga K, Nakamura M, Shinogami M, Tsuzuku T, Yamada K, Shindo M. Auditory nerve disease of both ears revealed by auditory brainstem responses, electrocochleography and otoacoustic emissions. Scand Audiol 1996;25:233–8.
Kanno A, Nakasato N, Fujita S, Seki K, Kawamura T, Ohtomo S, et al. Right hemispheric dominance in the auditory evoked magnetic fields for pure-tone stimuli. Electroenceph Clin Neurophysiol Suppl 1996;47:129–32.
Kanno A, Nakasato N, Murayama N, Yoshimoto T. Middle and long latency peak sources in auditory evoked magnetic fields for tone bursts in humans. Neurosci Lett 2000;293:187–90.
Khimich D, Nouvian R, Pujol R, Tom Dieck S, Egner A, Gundelfinger ED, et al. Hair cell synaptic ribbons are essential for synchronous auditory signaling. Nature 2005;14:889–94.
Kraus N, MacGee T, Ferre J, Hoeppner J, Carrell T, Sharma A, et al. Mismatch negativity in the neurophysiologic/behavioral evaluation of auditory processing deficits: a case study. Ear Hear 1993;14:223–34.
Mäkelä JP, Hämäläinen M, Hari R, McEvoy L. Whole-head mapping of middle-latency auditory evoked magnetic fields. Electroencephalogr Clin Neurophysiol 1994;92:414–21.
Meyer E, Michaelides M, Tee LJ, Robson AG, Rahman F, Pasha S, et al. Nonsense mutation in TMEM126A causing autosomal recessive optic atrophy and auditory neuropathy. Mol Vis 2010;16:650–64.
Michalewski HJ, Starr A, Nguyen TT, Kong YY, Zeng FG. Auditory temporal processes in normal-hearing individuals and in patients with auditory neuropathy. Clin Neurophysiol 2005;116:669–80.
Mizutari K, Matsunaga T, Inoue Y, Kaneko H, Yagi H, Namba K, et al. Vestibular dysfunction in a Japanese patient with a mutation in the gene OPA1. J Neurol Sci 2010;293:23–8.
Miyamoto RT, Kirk KI, Renshaw J, Hussain D. Cochlear implantation in auditory neuropathy. Laryngoscope 1999;109:181–5.
Morita T, Hiraumi H, Fujiki N, Naito Y, Nagamine T, Fukuyama H, et al. A recovery from enhancement of activation in auditory cortex of patients with idiopathic sudden sensorineural hearing loss. Neurosci Res 2007;58:6–11.
Näätänen R, Picton T. The N1 wave of the human electric and magnetic response to sound: a review and an analysis of the component structure. Psychophysiology 1987;24:375–425.
Nakasato N, Fujita S, Seki K, Kawamura T, Matani A, Tamura I, et al. Functional localization of bilateral auditory cortices using an MRI-linked whole head magnetoencephalography (MEG) system. Electroenceph Clin Neurophysiol 1995;94:183–90.
Nakasato N, Kumabe T, Kanno A, Ohtomo S, Mizoi K, Yoshimoto T. Neuromagnetic evaluation of cortical auditory function in patients with temporal lobe tumors. J Neurosurg 1997;86:610–8.
Nakasato N, Yoshimoto T. Somatosensory, auditory, and visual evoked magnetic fields in patients with brain diseases. J Clin Neurophysiol 2000;17:201–11.
Pantev C, Lutkenhoner B, Hoke M, Lehnertz K. Comparison between simultaneously recorded auditory-evoked magnetic fields and potentials elicited by ipsilateral, contralateral and binaural tone burst stimulation. Audiology 1986;25:54–61.
Pantev C, Bertrand O, Eulitz C, Verkindt C, Hampson S, Schuierer G, et al. Specific tonotopic organizations of different areas of the human auditory cortex revealed by simultaneous magnetic and electric recordings. Electroenceph Clin Neurophysiol 1995;94:26–40.
Rance G, Beer DE, Cone-Wesson B, Shepherd RK, Dowell RC, King AM, et al. Clinical findings for a group of infants and young children with auditory neuropathy. Ear Hear 1999;20:238–52.
Rance G, Cone-Wesson B, Wunderlich J, Dowell R. Speech perception and cortical event related potentials in children with auditory neuropathy. Ear Hear 2002;23:239–53.
Reite M, Zimmerman JT, Zimmerman JE. Magnetic auditory evoked fields: interhemispheric asymmetry. Electroencephalogr Clin Neurophysiol 1981;51:388–92.
Reite M, Adams M, Simon J, Teale P, Sheeder J, Richardson D, et al. Auditory M100 component 1: relationship to Heschl's gyri. Brain Res Cogn Brain Res 1994;2:13–20.
Romani GL, Williamson SJ, Kaufman L. Tonotopic organization of the human auditory cortex. Science 1982;216:1339–40.
Satya-Murti S, Wolpaw JR, Cacace AT, Schaffer CA. Late auditory evoked potentials can occur without brain stem potentials. Electroenceph Clin Neurophysiol 1983;56:304–8.
Singh G, Lott MT, Wallace DC. A mitochondrial DNA mutation as a cause of Leber's hereditary optic neuropathy. N Engl J Med 1989;320:1300–5.
Soeta Y, Nakagawa S. Sound level-dependent growth of N1m amplitude with low and high-frequency tones. Neuroreport 2009;20:548–52.
Starr A, McPherson D, Patterson J, Don M, Luxford W, Shannon R, et al. Absence of both auditory evoked potentials and auditory percepts dependent on timing cues. Brain 1991;114:1157–80.
Starr A, Picton T, Sininger Y, Hood LJ, Berlin CI. Auditory neuropathy. Brain 1996;119:741–53.
Starr A, Sininger YS, Pratt H. The varieties of auditory neuropathy. J Basic Clin Physiol Pharmacol 2000;11:215–30.
Starr A, Michalewski HJ, Zeng FG, Fujikawa-Brooks S, Linthicum F, Kim CS, et al. Pathology and physiology of auditory neuropathy with a novel mutation in the MPZ gene (Tyr145 -> Ser). Brain 2003;126:1604–19.
Starr A, Isaacson B, Michalewski HJ, Zeng FG, Kong YY, Beale P, et al. A dominantly inherited progressive deafness affecting distal auditory nerve and hair cells. J Assoc Res Otolaryngol 2004;5:411–26.
Sterling P, Matthews G. Structure and function of ribbon synapses. Trends Neurosci 2005;28:20–9.
Trussell LO. Synaptic mechanisms for coding timing in auditory neurons. Annu Rev Physiol 1999;61:477–96.
Varga R, Kelley PM, Keats BJ, Starr A, Leal SM, Cohn E, et al. Non-syndromic recessive auditory neuropathy is the result of mutations in the otoferlin (OTOF) gene. J Med Genet 2003;40:45–50.

Varga R, Avenarius MR, Kelly PM, Keats BJ, Berlin CI, Hood LJ, et al. OTOF mutations revealed by genetic analysis of hearing loss families including a potential temperature sensitive auditory neuropathy allele. J Med Genet 2006;43:576–81.
Vlastarakos PV, Nikolopoulos TP, Tavoulari E, Papacharalambous G, Korres S. Auditory neuropathy: endocochlear lesion or temporal processing impairment? Implications for diagnosis and management. Int J Pediatr Otorhinolaryngol 2008;72:1135–50.
Wienbruch C, Paul I, Weisz N, Elbert T, Roberts LE. Frequency organization of the 40-Hz auditory steady-state response in normal hearing and in tinnitus. Neuroimage 2006;33:180–94.

CELL STRUCTURE AND FUNCTION *Advance Publication by J-STAGE*

doi:10.1247/csf.12030

Received on: 2012/12/12
Accepted on: 2012/12/25
Released online on: 2013/01/11

Short Communication

Induction of neuritogenesis in PC12 cells by a pulsed electromagnetic field via MEK-ERK1/2 signaling

Tada-aki Kudo[1*], Hiroyasu Kanetaka[2], Yoshinaka Shimizu[3], Toshihiko Abe[4], Hitoshi Mori[4], Kazumi Mori[4], Eizaburo Suzuki[5], Toshiyuki Takagi[6], and Shin-ichi Izumi[5,7]

[1]*Division of Oral Physiology, Tohoku University Graduate School of Dentistry, 4-1 Seiryo-machi, Aoba-ku, Sendai 980-8575, Japan*

[2]*Liaison Center for Innovative Dentistry, Tohoku University Graduate School of Dentistry, 4-1 Seiryo-machi, Aoba-ku, Sendai 980-8575, Japan*

[3]*Division of Oral Pathology, Tohoku University Graduate School of Dentistry, 4-1 Seiryo-machi, Aoba-ku, Sendai 980-8575, Japan*

[4]*Institute of Field Generation, 1-14-9 Oritate, Aoba-ku, Sendai 982-0026, Japan*

[5]*Department of Physical Medicine and Rehabilitation, Tohoku University Graduate School of Medicine, 2-1 Seiryo-machi, Aoba-ku, Sendai 980-8575, Japan*

[6]*Institute of Fluid Science, Tohoku University, Katahira 2-1-1, Aoba-ku, Sendai 980-8577, Japan*

[7]*Tohoku University Graduate School of Biomedical Engineering, 2-1 Seiryo-machi, Aoba-ku, Sendai 980-8575, Japan*

Key words: electromagnetic field/PEMF/ERK1/2/neuritogenesis/PC12 cells

Running title: PC12 neuritogenesis by a PEMF

*To whom correspondence should be addressed: Tada-aki Kudo, Division of Oral Physiology, Tohoku University Graduate School of Dentistry, 4-1 Seiryo-machi, Aoba-ku, Sendai 980-8575, Japan.

Tel.: +81-22-717-8292, Fax: +81-22-717-8436

E-mail: tkudo@m.tohoku.ac.jp

ABSTRACT. **We examined the regulation of neuritogenesis by a pulsed electromagnetic field (PEMF) in rat PC12 pheochromocytoma cells, which can be induced to differentiate into neuron-like cells with elongated neurites by inducers such as nerve growth factor (NGF). Plated PC12 cells were exposed to a single PEMF (central magnetic flux density, 700 mT; frequency, 0.172 Hz) for up to 12 h per day and were then evaluated for extent of neuritogenesis or acetylcholine esterase (AChE) activity. To analyze the mechanism underlying the effect of the PEMF on the cells, its effects on intracellular signaling were examined using the ERK kinase (MEK) inhibitors PD098059 and U0126 (U0124 was used as a negative control for U0126). The number of neurite-bearing PC12 cells and AChE activity increased after PEMF exposure without the addition of other inducers of neuritogenesis. Additionally, PEMF exposure induced sustained activation of ERK1/2 in PC12 cells, but not in NR8383 rat alveolar macrophages. Furthermore, U0126 strongly inhibited PEMF-dependent ERK1/2 activation and neuritogenesis. The PEMF-dependent neuritogenesis was also suppressed by PD098059, but not U0124. These results suggest that PEMF stimulation independently induced neuritogenesis and that activation of MEK-ERK1/2 signaling was induced by a cell-type-dependent mechanism required for PEMF-dependent neuritogenesis in PC12 cells.**

Introduction

PC12 is a rat cell line derived from an adrenal pheochromocytoma and a useful model system for neurobiochemical and neurochemical studies (Radio and Mundy, 2008; Vaudry *et al.*, 2002). PC12 cells differentiate into neuron-like cells when exposed to various factors, including nerve growth factor (NGF) and bone morphogenetic proteins (BMPs) (Deutsch and Sun, 1992; Greene and Tischler, 1976; Koike *et al.*, 2006; Kudo *et al.*, 2011; Rydel and Greene, 1987).

The addition of NGF to PC12 cells causes sustained activation of extracellular signal-regulated kinases 1 and 2 (ERK1/2), members of the mitogen-activated protein kinase (MAPK) family, through activation of NGF receptor tropomyosin-related kinase A (TrkA). Sustained activation of ERK1/2 leads to neurite outgrowth and the development of phenotypic characteristics in PC12 cells (Kao *et al.*, 2001; Rakhit *et al.*, 2001). However, the mechanisms that link the activation of NGF receptors to neuritogenesis are not well-defined.

BMPs are members of the transforming growth factor (TGF)-β cytokine superfamily, which mediates multiple biological processes, including neuronal development (Wrana *et al.*, 1994). BMPs bind to two classes of transmembrane receptors (Hogan, 1996) and activate two downstream pathways, the Smad and p38 MAPK signaling pathways (Heldin *et al.*, 1997; Kimura *et al.*, 2000). BMPs have also been shown to induce neurite outgrowth in PC12 cells and neurons (Fantetti and Fekete, 2012; Iwasaki *et al.*, 1996). In the BMP-induced neuronal differentiation of PC12 cells, neuritogenesis is dependent upon BMP-mediated p38 MAPK signaling (Iwasaki *et al.*, 1999; Yanagisawa *et al.*, 2001).

While electromagnetic fields, including pulsed electromagnetic fields (PEMFs), are considered a noninvasive way to promote and align nerve regeneration (Schimmelpfeng *et al.*, 2005), their mode of action at the cellular and molecular levels is unclear. Previous studies indicate that the biological effects of PEMFs, with or without NGF, on neuronal or neuron-like cells appear to be dependent on the usage of a PEMF (Morgado *et al.*, 1998; Schimmelpfeng *et al.*, 2005; Zhang *et al.*, 2006). Few studies have investigated the molecular mechanisms of intracellular signaling in PC12 cells subjected to PEMF stimulation alone.

In light of the possible therapeutic applications of electromagnetic fields, we examined the likelihood of controlling neuritogenesis or acetylcholine esterase (AChE) activity, characteristics of a differentiation phenotype of PC12 cells (Greene *et al.*, 1981), with a single PEMF of 700 mT, pulsed for 0.04 ms in monophasic form at 0.172 Hz alone for various time periods in PC12 cells. The PEMF used in this study induced neurite outgrowth gradually and independently in PC12 cells. Here, we report the molecular characterization of PEMF-induced intracellular signaling and neurite outgrowth in PC12 cells and discuss a possible mechanism of action of PEMF.

Materials and Methods

Cells and reagents

PC12 cells and NR8383 rat alveolar macrophages were provided by RIKEN BRC and ATCC, respectively. Recombinant human BMP4 (Peprotech) and recombinant human β-NGF (Peprotech) were dissolved in LF6 buffer solution (5 mM glutamic acid, 5 mM

NaCl, 2.5% glycine, 0.5% sucrose, 0.01% Tween 80). The MEK1/2-specific inhibitors U0126 (Calbiochem) and PD098059 (Cayman Chemical Company), and a negative control for U0126, U0124 (Merck Millipore), were dissolved in dimethyl sulfoxide (DMSO).

Antibodies

Western blot analysis was performed as described previously (Kudo *et al.*, 2011). The following antibodies were used: anti-phosphorylated (activated) ERK1/2 and anti-ERK1/2 (Cell Signaling Technology).

Cell culture and the induction of differentiation

PC12 cells and NR8383 cells were maintained as described previously (Kudo *et al.*, 2011). For neurite outgrowth assays using PC12 cells, cells were seeded in growth medium at a density of 1×10^4, 2×10^4, or 6×10^4 cells/well in collagen type IV-coated 6- or 24-well culture plates (BD Biosciences) and allowed to grow for 24 h. Subsequently, the cells were serum-starved in DMEM supplemented with 1% horse serum and set on the coil of an electromagnetic stimulator (IMS101-50; Institute of Field Generation). Exposure to a single PEMF (magnetic flux density at the center of the coil, 700 mT; frequency, 0.172 Hz (duration of each cycle, 5.8 s); pulse duration, 0.04 ms; pulse form, monophasic) or a double PEMF (magnetic flux density at the center of the coil, 700 mT; frequency, 0.172 Hz (duration of one cycle, 5.8 s); interval between the two pulses, 0.5 s; pulse duration, 0.04 ms; pulse form, monophasic) was performed for various time periods

(0-12 h/day) for a maximum of 14 days according to the manufacturer's instructions. Alternatively, cells were treated with 40 ng/ml BMP4 or 50 ng/ml NGF as a positive control for neuritogenesis. For PEMF exposure lasting longer than 3 h, a 1-h break was programmed using a PT50DG digital timer (REVEX) to avoid overheating of the coil on the electromagnetic stimulator. Neuritogenesis was quantified by examining the cells using a DP72 phase-contrast microscope (Olympus). Three images per well were captured, and cells displaying projections 1.5 times longer than the length of the cell body were considered positive. At least 300 cells were counted per well; each data point corresponds to the counts obtained from three independent wells.

AChE assay

To evaluate AChE activity in PC12 cells, the choline produced from acetylcholine by endogenous AChE in each sample was quantified using an Amplite Fluorimetric acetylcholine esterase assay kit (AAT Bioquest) according to the manufacturer's instructions. For each sample, the signal was read using a microplate reader (GloMax-Multi Detection System; Promega) as the absorbance at 560 nm and normalized to the protein concentration.

Statistical analysis

The data are presented as the mean ± SE. Significant differences between groups were identified by Student's *t*-test or one-way analysis of variance followed by Tukey's test. *P*-values <0.05 were considered statistically significant.

Results and Discussion

To examine the effects of a PEMF on the neuronal differentiation of PC12 cells, we first investigated the dose effect of exposure to a single PEMF (see Materials and Methods for details) on neuritogenesis. PC12 cells were either incubated for 6 days in the presence of a positive control (40 ng/ml BMP4 or 50 ng/ml NGF) or exposed to the PEMF for various time periods (a total of 0.75, 3, or 12 h per day), and the extent of neurite outgrowth was evaluated. Neurite extension was less than 3% in PC12 cells incubated without stimulation for 6 days (Fig. 1A, G). Treatment with BMP4, an inducer of neuritogenesis in neurons (Fantetti and Fekete, 2012), induced neuritogenesis gradually by day 6 (Fig. 1E, G), although the effect was not as strong as that for NGF-induced neuritogenesis (Fig. 1F, H; Hayashi *et al.*, 2001). No significant enhancement of neurite outgrowth was observed on day 6 in PC12 cells exposed to the PEMF for 0.75 or 3 h (Fig. 1B, C, G). In contrast, exposure to the PEMF for 12 h significantly induced the outgrowth of neurite-like projections in PC12 cells in the absence of other neuritogenesis inducers, similar to the results for BMP4 (40 ng/ml) (Fig. 1D, G). The morphology of the neurite-like projections generated as a result of exposure to the PEMF for 12 h resembled that of the BMP4-induced neurites (Fig. 1D, E, G) and fewer neurites were observed on day 6 in PEMF-exposed or BMP-treated neurite-bearing cells than in NGF-treated cells (Fig1 D-F).

We next evaluated the time course of PEMF-dependent neuritogenesis in PC12 cells. We first scored PC12 cells exposed to the PEMF for 12 h for neurite outgrowth on the indicated days (days 0-7). As shown in Fig. 2A and F, prior to exposure on day 0, the cells